

Manuscript Template

Constraining the contribution of the Antarctic Ice Sheet to Last Interglacial sea-level

Authors: R.L. Barnett^{1,2,8}, J. Austermann^{3,8*}, B. Dyer⁴, M.W. Telfer⁵, N.L.M. Barlow⁶, S.J. Boulton⁵, A.S. Carr⁷, R.C. Creel³

Affiliations:

- 1. Geography, College of Life and Environmental Sciences, University of Exeter, Exeter, UK
- 2. Département de biologie, chimie et géographie et Centre d'études nordiques, Université du Québec à Rimouski, Rimouski, QC, Canada
- 3. Lamont Doherty Earth Observatory, Columbia University, Palisades, NY, USA
- 4. School of Earth and Ocean Sciences, University of Victoria, Victoria, BC, Canada
- 5. School of Geography, Earth and Environmental Sciences, University of Plymouth, Plymouth,
 UK
 - 6. School of Earth and Environment, University of Leeds, Leeds, UK
 - 7. School of Geography, Geology and the Environment, University of Leicester, Leicester, UK
 - 8. These authors contributed equally

*Corresponding author: jackya@ldeo.columbia.edu

Teaser:

Sea-level data from a past warm period (the Last Interglacial) are used to constrain the past (and potential future) contribution of the Antarctic Ice Sheet to multi-meter global sea-level rise.

Short title: Antarctic Ice Sheet change during the Last Interglacial

Abstract

Polar temperatures during the Last Interglacial (LIG; ~129-116 ka) were warmer than today, making this time period an important testing ground to better understand how ice sheets respond to warming. Yet it remains debated how much and when the Antarctic and Greenland ice sheets changed during this period. Here we present a combination of new and existing absolutely dated LIG sea-level observations from southwest Britain, northern France, and Denmark. Due to glacial isostatic adjustment (GIA), the LIG Greenland ice melt contribution to sea-level change in this region is small, which allows us to constrain Antarctic ice melt. Combining data and GIA modelling, we find that the Antarctic contribution to LIG global mean sea level peaked early in the interglacial (prior to 125 ka), with a maximum contribution of 5.6 m (50th percentile, 3.3–8.8 m central 68% probability) before declining. Our results support an asynchronous melt history over the LIG, with an early Antarctic contribution followed by later Greenland ice-sheet mass loss.

MAIN TEXT

Introduction

8 9

0

1

2

3

5

7

0

1

It is extremely likely that global temperatures will be 2°C warmer than pre-industrial levels by 2100 (1). While predictions of emissions and temperature are somewhat well constrained and depend on Representative Concentration (2) or Shared Socioeconomic (3) Pathways, the sea-level response to different amounts of warming is less certain (4). Furthermore, a greater understanding of the complexities of ice-Earth-ocean processes associated with ice sheets has increased uncertainty in sea-level projections in the AR6 IPCC report (4) compared to earlier reports. The current likely range (central 68% probability) of global mean sea-level (GMSL) rise by 2100 from low- (SSP1-4 2.6) to high- (SSP5-8.5) end scenarios is 0.33-1.02 m (4), but this range increases significantly when the potential effects of marine ice-cliff instability in Antarctica are considered (5, 6). As mass loss from the Greenland Ice Sheet (GIS) and mountain glaciers closely track temperature, their futures largely depend on emissions scenario (7). However, the Antarctic Ice Sheet (AIS) is susceptible to dynamic instabilities from calving (8), grounding line retreat (9), basal melting (10), hydrofracturing (11), marine-ice sheet instability (12) and potentially marine ice-cliff instability (11) – effects that mean the ice sheet response to future warming is poorly understood (13). This deep uncertainty surrounding nonlinear instabilities of the AIS dominates the uncertainty in sea-2 level projections (5), limiting their usability for managing coastal risk (14).

3

5

6

9

0

1

3

4

5

6

8 9

0

1

2

Paleo sea-level data from past warm periods, when GMSL was meters higher than present, can yield crucial insights into how the AIS will respond to warming (15). The LIG period is characterized by warmer than present polar temperatures (16, 17) and GMSL 5 to 10 m higher than present day (4, 15). These characteristics are therefore useful for understanding future sea-level rise (6, 18, 19). However, in general there remains low agreement in LIG GMSL related to its magnitude (e.g. 6.6-9.4 m based on a global data compilation (20) to 1.2-5.3 m based on data from the Bahamas (21), timing (e.g. sea level peak early in the LIG in the Seychelles (22) and Red Sea (23) versus late in Western Australia (24)), structure (e.g. unimodal (25), dual-peaked (20), or multi-2 peaked (23)) and melt source (GIS or AIS (4)). Currently, constraints for the Antarctic contribution to LIG GMSL have been inferred from relative sea-level (RSL) curves from single regions (e.g. the Seychelles (6)) or probabilistic assessments of globally distributed datasets (20). To estimate the GMSL contribution from Antarctica, the contributions from all sources (e.g., solid Earth, Greenland, Antarctica, glaciers and thermal expansion) must be deconvolved from LIG RSL curves, which requires assumptions about each source, particularly the magnitude of GIS mass loss. Most LIG RSL data come from sites in the intermediate- and far-field of (i.e., distal to) Late Pleistocene ice sheets. However, these locations undergo RSL changes driven by mass loss from both the AIS and GIS (26), which makes distinguishing the relative contributions from the different ice sheets challenging (27). There is a pressing need for an observationally constrained estimate of the Antarctic contribution to LIG GMSL to better parameterize next generation GMSL projections, and new data from near-field locations provide this opportunity (15, 28).

3 4 5

6

8

9

0

1

2

3 4

5

Here we present a new LIG RSL reconstruction for northwest (NW) Europe, a region whose proximity to Greenland makes local sea-level changes not very sensitive to GIS mass loss, particularly in the early LIG (26, 28), but very sensitive to mass loss from Antarctica (Fig. 1a,b). We report new geochronological controls for three LIG coastal sites in southwest (SW) Britain and compile a database of absolutely dated (i.e., ages are not inferred through relative techniques) LIG coastal features from a further thirteen sites across NW Europe (Fig. 1; Supplementary Data). Working within a near-field region raises the challenge of large uncertainties in the GIA correction associated with Late Pleistocene ice mass changes, here the Eurasian Ice Sheet (29, 30) (Fig. 1c,d). However, our database allows us to reduce the GIA uncertainty by leveraging spatial trends within our data to identify the most likely GIA scenarios within a large range of model runs (n = 576; Materials and Methods). We estimate long-term deformation due to mantle dynamic topography

(31), crustal deformation, or sediment loading (32) using Pliocene marine platforms at each site assuming constant uplift rates. Our data, long-term deformation estimates, and GIA models are combined within a Bayesian framework to infer a regionally self-consistent estimate of the glacial GIA-corrected sea-level (see Materials and Methods). We emphasize that 'glacial GIA-corrected' refers to GIA corrections related to ice changes before and after, but not during, the LIG. We account for that contribution (interglacial GIA correction) separately by modelling the local sea-2 level response to a range of GIS melt scenarios during the LIG. The glacial GIA-corrected sea-level estimate, with subtraction of the sea-level contributions from Greenland, mountain glaciers and thermal expansion, results in a new observationally constrained estimate of the Antarctic contribution to GMSL during the LIG. It is possible that the Laurentide ice sheet was still present during the early LIG (33), in which case this procedure yields a lower bound for the Antarctic contribution to LIG GMSL.

Results and Discussion

1 2

Coastal sea-level indicators

We present new absolute age constraints for three LIG coastal sequences in SW Britain using optical dating of quartz and K-feldspar sand grains (Materials and Methods). The coastal sequences belong to the Godrevy Member of the Penwith Formation (34) and comprise LIG littoral deposits that occupy (interglacial) wave-cut platforms in Devon and Cornwall (35, 36). Basal intertidal pebble-beach foreshore facies are overlain by sandy-beach backshore deposits that, in some locations, grade upwards into dune sands. Samples from the basal contacts of the sandy-beach backshore deposits at all sites (4.4–6.4 m ODN; Ordnance Datum Newlyn) date to Marine Isotope Stage (MIS) 5e (i.e., 1σ age uncertainties overlap with 129-116 ka) (Table 1; Supplementary Data). Two further samples of cemented beach sands unconformably overlying shore platforms with wave-cut notches at elevations of 4.4 and 4.7 m ODN date to late MIS 5e. To estimate local RSL in SW Britain, we correct sample elevations for reference water levels of the associated depositional features and calculate error terms from the indicative ranges of the depositional features (37) (Materials and Methods, Supplementary Data). The documented beach facies record the elevation of maximum RSL from which we resolve the mean weighted local LIG RSL highstand in SW Britain to 4.9 ± 1.0 m (1σ).

Our results are compiled into a dataset of LIG RSL features (e.g. marine sediments, beach facies, dune sands) from across NW Europe (Table 1; Supplementary Data), following established protocols (37). We limit the dataset to data derived from absolute-dating approaches synonymous to our new age constraints (i.e. luminescence, uranium-series), but recognize that this necessitates an omission of data from age-inferred approaches (e.g. pollen zone associations (38)). The dataset includes MIS 5e beach deposits in NW France (mean weighted age 118 ± 7 ka, 1σ) that constrain the RSL highstand there to 4.6 ± 1.2 m (1σ). Relatively younger dune sands overlying these beach facies indicate RSL fall and limit the height of RSL to ≤ 2.7 m during late MIS 5e (112 ± 7 ka, 1σ) and ≤ -3.0 m during MIS 5d (107 ± 7 ka, 1σ). The dataset also includes RSL estimates and terrestrial limiting data points for southern Britain, the Channel Islands and Denmark (Table 1). Given that the limiting data do not allow us to constrain the height of RSL as their elevation of formation may be significantly above the highest tides, and their potential ages outside the MIS 5e range, we did not include limiting data in our sea level modeling.

Glacial GIA-corrected sea level in NW Europe

Science Advances Manuscript Template Page 3 of 29

1 2

To correct the LIG sea-level database for GIA we consider two contributions: (1) GIA driven by ice mass changes prior to and after the LIG, and (2) GIA driven by ice mass change during the LIG. The first component is assumed to cause the majority of the spatial variability in sea level in this region (Fig. 1). Using a suite of 576 different glacial GIA models therefore allows us to quantify the common sea level signal in NW Europe, which we call 'glacial GIA-corrected sea level'. In a second step we consider how much of this regional sea level signal is driven by Greenland versus Antarctic ice change during the LIG (accounting for both their GMSL and GIA contribution). Our suite of glacial GIA models represents six ice-sheet configurations with varying sea-level equivalent (SLE) ice volumes in the Eurasian Ice Sheet ranging from 23 m (i.e. equivalent to Last Glacial Maximum, LGM, configuration (39)) to 70 m (40) during the penultimate glacial maximum (Fig. S1). Each scenario is paired with two penultimate deglaciation rate pathways and uses modern ice extent over the course of the LIG. A glacial GIA prediction is generated by calculating the gravitationally self-consistent sea-level response to ice and water mass load changes on a rotating Earth (41) for the varying ice-sheet and Earth model parameters (48 variations of Earth lithosphere thickness and upper- and lower-mantle viscosities, see Materials and Methods).

Beyond GIA effects, the elevation of LIG sea-level indicators can change after deposition due to crustal deformation from tectonics, offshore sediment loading (32), and mantle dynamic topography (31). We account for the collective effects of this long-term deformation by using the elevation of co-located Pliocene marine platforms (Materials and Methods). We employ a Bayesian framework to infer the most likely sea-level curve by calculating the most likely posterior estimates for GIA and long-term deformation given the spatial and temporal distribution of the RSL data, with prior knowledge specified via the range of GIA models and long-term deformation rates described above.

By considering the posterior glacial GIA weights, we are able to infer the more plausible ice-sheet histories and Earth structures identified by the Bayesian inversion. The inversion tends to favor glacial GIA models with Eurasian Ice Sheet geometries containing between 24 m and 47 m SLE ice volumes (Fig. S2), suggesting that ice volume in Eurasia during the penultimate deglaciation may have been similar to or greater than ice volumes during the LGM. This is at the lower end of a recent estimate based on ice sheet modeling (42). We find that it is unlikely that the Eurasian Ice Sheet contained a SLE of 71 m as suggested by some ice models (40). The inversion favors 'slow' deglaciation rates (i.e., starting around 140 ka instead of 135 ka; Fig. S2), unless paired with a small Eurasian Ice Sheet (i.e., 24 m SLE), in which case relatively faster deglaciation rates are more likely. In terms of Earth structure, the inversion shows little preference for lithosphere thickness (i.e., 48 km, 71 km, or 96 km) or upper mantle viscosities, but tends to favor lower mantle viscosities < 15 x 10^{21} Pa s.

Our glacial GIA-corrected sea-level estimate shows a high sea level in NW Europe early during the LIG, followed by a gradual fall after 126 ka (Fig. 2a). The posterior RSL curves for locations in NW Europe (Fig. 2b-d) differ from the glacial GIA-corrected sea-level estimate because they include the significant glacial GIA effect in the region (Fig. 1c, d). LIG RSL falls in Denmark over the course of the LIG (Fig. 2b) due to crustal rebound. In contrast, RSL peaked late during the LIG in SW Britain (Fig. 2c) and NW France (Fig. 2d) due to GIA subsidence. Note that the large age uncertainties of our RSL data limit our ability to resolve rates of change during MIS 5e. Next, we leverage the low sensitivity of the region to mass loss from Greenland to derive an estimate of the Antarctic contribution to our glacial GIA-corrected sea-level estimate for NW Europe.

Antarctic contribution to LIG global mean sea level

8

1

3

4

5

7

8

9

0

2

3

4

To estimate the Antarctic contribution to LIG GMSL, we first subtract the effect that Greenland ice change has on sea level in NW Europe. Using Greenland LIG climate-ice sheet models with SLE contributions varying from 0.6 m (43) to 5.1 m (44) (Fig. 3a, S3), we calculate the regional sea-0 level expression of these ice histories in NW Europe by accounting for Earth's gravitational, rotational, and deformational response to GIS mass loss. Using the same suite of 48 viscosity models from the Bayesian inversion allows us to produce probability distributions for the Greenland contribution to glacial GIA-corrected sea level in NW Europe (Fig. 3a). As expected from the elastic fingerprint prediction (Fig. 1b), initial mass loss from Greenland leads to only a very small increase in sea level. However, after a few thousand years, viscous deformation starts to counteract the gravitational signal leading to increased local sea-level rise in NW Europe (Fig. 3a, S3). The Greenland sea-level signal in NW Europe significantly lags GIS mass loss and the magnitude of mean sea-level rise in NW Europe is significantly smaller than the total SLE mass loss from the ice sheet. Taking the mean local sea-level response across all ice and Earth models suggests that the mean Greenland contribution to sea level in NW Europe is < 1 m and largely occurred during the second half of the interglacial. We note, however, that the magnitude could be up to 3m at the end of the LIG for an end-member ice history and earth structure combination (see Fig. S3). In either case, the majority of the glacial GIA-corrected sea-level signal early during the LIG (Fig. 2a) is attributable to other processes, most importantly mass loss from Antarctica.

5 Subtracting the time-varying Greenland contribution from our glacial GIA-corrected sea-level estimate results in a signal that is the combination of the Antarctic and mountain glacier contribution 6 as well as thermal expansion (Fig. 3b) assuming that the Laurentide ice sheet had melted by 128ka. 7 We next correct for contributions from thermal expansion $(0.30 \pm 0.22 \text{ m}, 1\sigma)$ (45) and mountain 8 glaciers $(0.32 \pm 0.08 \text{ m}, 1\sigma)$ (46) assuming that contributions are constant over the LIG. Finally, we 9 correct for the GIA effect of AIS mass loss during the LIG to estimate the Antarctic contribution to 0 LIG GMSL. The elastic fingerprint for West and East Antarctic mass loss is close to 1.05 in NW 1 Europe (Fig. 1a) (26), but the full GIA effect of LIG AIS change depends on the timing and location 2 3 of mass loss. Here we assume a GIA effect of LIG AIS change of $1.05 \pm 0.05\%$ (1 σ) and, as for thermal expansion and mountain glacier contributions, assume a constant value over the LIG. This 4 results in an Antarctic contribution to LIG GMSL that peaked at 5.6 m (50th percentile) (3.3 to 8.8 5 m; central 68% probability; Fig. 3e). This peak *likely* occurred at the beginning of the LIG prior to 6 127.8 ka (68% probability; Fig. 3f) before the Antarctic contribution decreased. 7

There is remarkable agreement between our estimate of the Antarctic contribution to GMSL during 8 the LIG and the reconstructed SLE ice loss in the Southern Hemisphere from a probabilistic 9 0 assessment of a globally distributed dataset (20) (Fig. 3c), however we note that our data put a tighter constraint on this quantity. Our study strongly favors early Antarctic ice loss with significant 1 ice regrowth over the course of the LIG, which agrees with some (47) but not all (19, 48) Antarctic 2 ice sheet models (Fig. 3c). Our central estimate is in excellent agreement with the LIG target range 3 of Antarctic SLE ice loss (3.1–6.1 m) used to parameterize sea-level projection models (6). This 4 target range is based on an LIG GMSL estimate from the Seychelles of 4.2–7.6 m (22) paired with 5 the assumption that Greenland had a limited contribution to an early LIG GMSL highstand. We 6 note that our estimate does not require this assumption. A recent re-analysis of Bahamian LIG sea 7 level indicated that GMSL peaked early in the LIG and very unlikely exceeded 5.3 m (21). If true, 8 this would require a peak Antarctic contribution on the lower end of our estimated range (i.e., less than 4.4 m if we assume a fingerprint factor of 1.2 for the Bahamas, Fig 1a, and no early-LIG mass 0 1 loss from Greenland). However, recent evidence that the Laurentide ice sheet may have persisted into the LIG (33) would imply that our estimates represent a minimum of the early LIG Antarctic 2 contribution. 3

Science Advances Manuscript Template Page 5 of 29

We note that the lower bound of our central estimate of the Antarctic contribution to LIG GMSL (3.3 m; 16th percentile) corresponds closely to potential GMSL rise from collapse of the vulnerable parts of the present-day West Antarctic Ice Sheet (3.2 m) (49). In other words, based on our results, there is a less than 16% probability that the WAIS can account for the entire Antarctic contribution to GMSL rise during the LIG. Regardless of whether there was substantial (50) or limited (51) mass loss from the WAIS during the LIG, our results suggest that additional contributions from other Antarctic sources are likely needed to explain the LIG GMSL highstand (84% probability). While rapid rebound of the bedrock under the WAIS can contribute up to 1 m of GMSL rise from the outflow of meltwater from the continental interior (52), this signal is likely smaller during the LIG (53). Our results therefore indicate that parts, if not all, of WAIS melted during the Last Interglacial or by the end of the penultimate glacial termination, which makes it likely that these sectors will also contribute to sea-level rise in the future.

Materials and Methods

4

5

6

7

8

9

0

1

2

4

5

0

1

2

3

4

5

8 9

0

1

2

3

4 5

6

7

8

9

1 2

3

4 5

6

7

8

9

0

Northwest Europe sea-level database

A database of absolutely-dated LIG sea-level indicators from across Northwest (NW) Europe was constructed using new (this study) and published dates (Supplementary Data). To ensure that coastal deposits are associated with the LIG, the database is restricted to dates derived from absolute-dating techniques (in this case, from optically stimulated luminescence, thermoluminescence, and uranium-series techniques) and only those dates with constrained ageuncertainties that overlap with MIS 5e/5d (i.e. 130-110 ka) (54) are accepted. All dates derive from littoral deposits associated with marine transgression during MIS 5e (e.g., beach sands and gravels, fine-grained estuarine sediments) or marine regression during MIS 5d (e.g. aeolian sands capping littoral deposits). The database comprises 20 sea-level index points (SLIPs) with defined vertical and temporal uncertainties, and 7 terrestrial-limiting (i.e., sea level is known to be lower than a defined elevation) points. References to all original data sources are provided in the Supplementary Data. Where multiple dates from a single facies are given (e.g. as in Jutland, Denmark and Sewerby, UK, a weighted mean and weighted uncertainty is calculated to provide a single chronological control for that facies. The database records environmental depositional interpretations of dated facies to support the calculation of reference water levels and indicative ranges. Dates from Jutland, Denmark, derive from intertidal beach deposits and overlying shoreface-glaciofluvial sands. Dates from five sites across Normandy in France derive from intertidal beach and beach ridge deposits and overlying aeolian dune sands. Published dates from the UK represent intertidal beach, beach ridge, marine and estuarine sediments and aeolian dune sands from sites in South Wales, Yorkshire, Sussex Devon, Cornwall, the Isle of Wight, and Jersey. We do not recalculate ages with updated decay constants, however, updates would be small compared to the age uncertainty. The database includes documented elevations of the basal and upper contacts for each dated facies. A uniform 0.4 m uncertainty is assigned to each contact elevation to account for variability across survey techniques and for the spatially variable height of the contacts (37).

Luminescence analytical methods

To improve temporal and spatial constraints on Last Interglacial (LIG) sea level in SW Britain, we present new dates from three key sites across Cornwall: the Godrevy Heritage Coast (50.25°N, 5.40°W), Bream Cove (50.11°N, 5.09°W), and Pendower (50.20°N, 4.94°W). The sites

have well-documented lithologies (36, 55-58) and are inferred to represent LIG transgressive regressive sequences, but to date have lacked absolute age controls.

Site Descriptions

Godrevy is the type-site for the Godrevy Member LIG coastal sequence in the region (35, 55) and comprises a 12 m thick stratotype between 4 and 16 m ODN (Ordnance Datum Newlyn) along an 800 m exposure. The sequence sits unconformably on a wave-cut platform incised into the Mylor Slate Formation. The base of the stratotype (between 4 and 6 m ODN) comprises three distinguishable sub-facies composed to varying degrees of a clast-supported conglomerate of well-rounded pebbles, cobbles and boulders within a coarse to medium-grained sand matrix and medium to coarse-grained sands containing occasional well-rounded pebbles. All basal sub-facies are interpreted as high-energy beach foreshore deposits (such as shingle cusps), and are overlain by well-indurated structurally variable (commonly horizontally bedded) well-sorted fine to medium-grained ferruginous sands with occasional rounded pebble clasts. These are interpreted as beach backshore sand deposits that mark the transition between the foreshore sub-facies below and fine, well-sorted dune sands above. Samples (n=4) from sand-rich facies were obtained for optically stimulated luminescence (OSL) dating (59) using opaque steel tubes.

The tidal notch at the northernmost end of the exposure at Godrevy was recently reexposed due to winter storms (60), and was levelled at two locations close to Godrevy Point at 5.9 \pm 0.2 m ODN and 6.1 \pm 0.2 m ODN, and one sample (GOD12-1) came from a small section of overlying sediments that represent transitional backshore beach deposits. This sample, however, returned an anomalously low equivalent dose, and although the site was revisited in 2017, this part of the section has now been removed by coastal erosion and reanalysis was not possible. The remaining three samples (GOD12-2/3/4; UK14-16) were obtained from the beach backshore sands immediately overlying the high-energy beach foreshore deposits at elevations of 6.7 m, 6.3 m, and 5.2 m ODN and distances 210 m, 220 m, and 260 m southward along the exposure from GOD12-1. All elevation surveying was conducted with a Trimble R10 real-time kinematic Global Navigation Satellite System (RTK-GNSS).

Samples of the Godrevy Member beaches were also taken at Bream Cove and Pendower. At these sites, the LIG sequences sit unconformably on top of wave-cut sandstone and slate platforms belonging to the Portscatho Formation (61). Basal facies of rounded clast-supported (pebble to boulder) conglomerates containing medium to coarse sands grade into well-sorted medium ferruginous sands containing well-rounded pebble horizons of variable matrix- to clast-supported texture and are analogous to the beach foreshore-backshore facies associated with the Godrevy Formation. Wave-cut notches are present within the fossil platforms at both sites (57, 62). The intermittent notches at both sites contain cemented beach foreshore sands, which were sampled for luminescence dating (PEN13-1 and BRM13-2; UK11 and UK13). The notch at Bream Cove has a maximum levelled elevation of 4.7 m ODN and occurs discontinuously over 200 m (56) in association with the basal beach foreshore deposits. The tidal notch in the platform at Pendower has a maximum levelled elevation of 4.4 m ODN (58). RTK-GNSS surveying confirmed the elevation of the sequences sampled with reference to the notch height. Samples for luminescence dating also came from the well-sorted backshore sands immediately overlaying the 2 beach basal facies (PEN13-2 and BRM13-1; UK10 and UK12).

Sample Preparation

Samples for luminescence dating were taken using plastic or steel tubes. Sample preparation for equivalent dose (D_e) determination followed conventional protocols (63, 64); sieving a fraction within 90-250 µm, H₂O₂ and HCl treatment to remove organic matter and carbonates (respectively), density separation with sodium polytungstate at 2.72 g cm⁻³ to remove heavy minerals and at 2.58 g cm⁻³ to isolate K-rich feldspars and finally (for the quartz fraction)

etching with 40% HF to remove feldspars and the alpha-irradiated rind of quartz grains. Given the low yields of K feldspar grains the < 2.58 g cm⁻³ fraction was not etched prior to analysis.

Environmental dose rates

9

0

1

3

4

5 6

8 9

0

1

2

3

4 5

6

7 8

9

1

2

3

4

5

6

7

8

9

0

2

3

4

5

6

7

8 9

0

1

3

4

Dosimetry was provided via in-situ gamma spectrometry using a Canberra Inspector 1000TM with a 2" NaI detector, inserted directly into the holes from which the samples were taken. From these measurements the concentration of the radionuclides U, Th and K were determined using the "windows" method (65), and the resulting alpha, beta and gamma dose rates derived following appropriate correction for grain size, water content and HF etching (following (66, 67)). Uncertainties were assumed at a conservative 5% for K, and 10% for U and Th, including counting uncertainties. For the unetched K-feldspar samples, an 'a-value' of 0.1 was assumed for calculating the alpha dose (following (68)). For K-feldspar measurements, the doses from internal K and Rb assume K-feldspar grain K and Rb concentrations of 12.5 \pm 0.5 % and 400 ± 100 ppm respectively (69, 70). Average burial water contents were based on the modern (measured) contents. Given the risk of drying of the sediments when exposed in the sections and after sampling, a water content uncertainty (1 σ) of 5 (absolute) % was applied to the dose rate calculations. As a measure of the sensitivity of the ages to a change in water content, a 1% change in absolute water content results in a 0.99 % difference in sample age for the quartz results, and a 0.98 % difference for the K-feldspar ages. The use of K feldspars for dating militates against this issue somewhat, due to the additional internal dose rate contribution. Cosmic dose rates were calculated following (71) and assuming an overburden equivalent to the modern beach sediment height.

Quartz Optically Stimulated Luminescence measurements

Luminescence measurements were made using small (2 mm) aliquots of quartz and a Risoe DA20 TL/OSL reader. Stimulation (60 s at 125°C) was provided by blue LEDS (stimulation wavelength 470 nm) at 70% power (delivering ~ 72 mW cm⁻² to the sample). OSL signals were detected with an EMI 9235QA photomultiplier tube with a U-340 detection filter. Laboratory irradiations were delivered by a calibrated ⁹⁰Sr beta source with dose rates (at the time of measurement) of 8.36 Gy min⁻¹ (Godrevy) and 8.75 Gy min⁻¹ (Pendower and Bream Cove). Equivalent doses (D_e) were determined using the single aliquot regeneration protocol (SAR) (72, 73). All analyses comprised 6 - 8 regeneration point sequences, including a zero dose (to assess recuperation) and in most cases two "recycling" (repeat) dose points (low (34 Gy) and high (237 Gy)). For all samples, the suitability of the SAR protocol and appropriate measurement (preheating) conditions were determined using preheat plateau experiments and dose recovery experiments (73). For the latter, samples were bleached twice with blue LEDs (with a 10,000 second pause in between) prior to laboratory beta dosing.

Analyses were carried out in the Analyst software package (74). OSL Signals were integrated using the first 0.5 seconds and an early (0.5-1.2s of stimulation time) background subtraction (75). The resulting dose response curves were fitted with saturating exponential plus linear curves and equivalent dose uncertainties were estimated using a Monte Carlo simulation method (74). Final equivalent dose uncertainties incorporate a systematic instrument error (1.5%) and beta dose rate uncertainty (3%) (76). The central age model of Galbraith, Roberts, Laslett, Yoshida and Olley (77) was used to derive a single D_e estimate.

K-feldspar Infrared Stimulated Luminescence (IRSL) measurements

In light of the relatively insensitive quartz OSL signal at Pendower in particular (Fig. S4), and the magnitudes of quartz equivalent doses in general, additional IRSL measurements were made on the K feldspar fractions from Bream Cover and Pendower. These employed the post IR-IRSL (pIRIR) measurement protocol (78, 79). This method seeks to mitigate the issue of

anomalous fading in K feldspars (80, 81) by isolating a non-fading (or more slowly fading) IRSL signal and involves an initial low temperature IRSL measurement (typically at 50°C) to evict the most fading-prone electrons, followed by a higher temperature IRSL measurement ("post IR") that accesses a less fading-prone signal, from which an equivalent dose is derived (79, 82). The latter IR stimulation is typically carried out at 225°C (pIRIR₂₂₅) (78) or 290°C (pIRIR₂₉₀) (79). In each case equivalent dose determination involves a modified Single Aliquot Regeneration (SAR) protocol (72, 83), with 250 and 320°C preheating temperatures used for the pIRIR₂₂₅ and pIRIR₂₉₀ (respectively) protocols. Here pIRIR K-feldspar measurements were made on small (2 mm) aliquots. Stimulation was provided by IR diodes (wavelength 870 nm), with detection of the resulting (blue-violet) IRSL through a combination of Schott BG39 filters and Corning 7-59 filters (detection range 320 - 450 nm). All SAR analyses comprised a 6 regeneration point sequence, including a zero dose. The IRSL signals were derived from the first 10 seconds of stimulation, with a background subtraction derived from the last 4 seconds of measurement. All dose response curves were well fitted with a saturating exponential fit in the Analyst software.

Dating results

Quartz

The Godrevy and Bream Cove samples generally produced rapidly decaying OSL signals (Fig. S4), and exhibited low levels of signal recuperation, reproducible growth curves (low numbers of recycling ratio rejections for both high and low dose recycling points) and satisfactory dose recovery (Table S1). Both the Godrevy and Bream Cove samples showed little sensitivity to the choice of preheating temperature (Figure S5). Together, these observations imply suitability of the SAR protocol for quartz. In contrast, the Pendower samples, particularly PEN13-2, were characterised by low OSL sensitivities (Fig. S4), and despite the use of early background signal subtraction, up to 25% of aliquots exhibited unacceptable levels of signal recuperation, as well as high recycling ratio rejection rates.

Three Godrevy samples produced quartz OSL ages within uncertainties of one another (Table S2) and all ages fall within the range of MIS 5e. Both the Godrevy and Bream Cove samples exhibited equivalent doses in excess of 150 Gy, although the samples exhibit growth in sensitivity-corrected OSL beyond 390 Gy (Fig. S4). Nonetheless, these equivalent doses are relatively high compared to the expected saturation point of the quartz fast component, and fall within a De range for which age underestimation has in some instances been reported (e.g. (84-8 86)), albeit not in all cases (e.g. (87, 88)).

We evaluated the proximity to saturation further by considering the dose-response curves obtained when fitting a single saturating exponential fit of the form: I = I0(1-exp[-D/D0]), where I is the luminescence intensity, I0 is the saturation intensity, D is the dose (Gy) and D0 (Gy) is the "characteristic dose". The characteristic dose parameter D0 provides a measure of the degree of saturation whereby 2 x D0 is equal to ~87% of saturation and is often considered a prudent measure of an aliquot's proximity to saturation (e.g. (89)). For most aliquots the saturating exponential fit provided an adequate characterisation of the dose response, and equivalent doses with finite uncertainties could be estimated. CAM equivalent doses also did not differ significantly from those obtained when using a saturating exponential plus linear fit, except for GOD-4 (in this instance 207 ± 11 Gy vs. 243 ± 13 Gy). The ratio of De to D0 for the three Godrevy samples (dosed to 404 Gy) was 2.2 ± 0.6 , 2.5 ± 0.5 , 2.1 ± 0.7 (mean ratio and standard deviation for GOD-2, GOD-3 and GOD-4 respectively). For three of the 17 measured GOD-3 aliquots it was not possible to interpolate an equivalent dose and/or finite equivalent dose uncertainty using a single saturating exponential fit. For BRM, the De/D0 ratios are lower (2.0 ± 0.7 and 1.6 ± 0.9), but still quite close to the 2D0 threshold.

Science Advances Manuscript Template Page 9 of 29

These data suggest the samples are potentially close to the limits of the quartz SAR method. However, as shown below, for BRM the quartz ages are entirely consistent with the K-Feldspar results, implying that a De/D0 ratio ~1.5-2.0 does not necessarily preclude a reliable quartz age estimate. Unfortunately, the Godrevy K-feldspar fractions were not available for analysis, precluding a comparable check. However, given the sample context, pending further analysis, we consider the present Godrevy quartz ages to be parsimonious.

Inter-aliquot scatter was low (overdispersion, *sensu* (77) of 11-19%) (Figs. S6 and S7). For both Bream Cove and especially Pendower, however, calculated equivalent doses from quartz resulted in more widely-dispersed age estimates, with higher overdispersion (i.e., inter-aliquot scatter) of 20-27%. In the case of Pendower, the quartz OSL ages were also stratigraphically inverted.

IRSL dating

4

5

6

7

8 9

0

1

3

4 5

6

7

8

9

0

1

2

3

4 5

6

7

8

9

0

1

2

3

4 5

6

7

8 9

0

1

2

4

5

6

7

9

0

1

pIRIR estimates were obtained for the Pendower and Bream Cove K-feldspar fractions (<2.58 g cm⁻³). K-feldspar yields were very low, which limited the number of analyses that could be undertaken. Unfortunately, the Godrevy K-feldspars fractions were lost in initial quartz preparations. In all samples the residual IRSL signal was tested following 48 hours of daylight exposure, while the suitability of the pIRIR SAR protocol was also assessed via several dose recovery experiments. For Bream Cove, although the pIRIR₂₂₅ (78) protocol produced negligible fading rates (g-value ~1% per decade) the residual ("unbleachable") signal remaining after 2 days of daylight exposure was ~20 Gy (Table S1), which amounts to 8-9% of the sample equivalent dose. The residual doses increased substantially with the pIRIR₂₉₀ method. Dose recovery results for the pIRIR₂₂₅ method were acceptable given the measurement uncertainties (Table S1). A lower temperature (170°C) second IR stimulation and a commensurately lower preheating temperature (i.e. 200°C; (90-92)) reduced the residual signal (to 12-17 Gy or 5-6% of the sample D_e; Table S1). The fading rate also remained relatively low (g value < 1.5% per decade – see below). We therefore derived all K feldspar equivalent doses using the pIRIR₁₇₀ protocol, with no measured residual subtracted from the final equivalent dose estimate. The K feldspar equivalent doses for the Bream Cove and Pendower samples are shown in Table S2. In all cases growth in the sensitivity-corrected IRSL signal continued beyond 400 Gy (Fig. S8) and the equivalent dose distributions showed low over-dispersion (0-8%; Fig. S9). Fading rates (following (93)) determined following administration of a 35 Gy beta dose and with measurement delays ranging from 0.1 to 185 hours were 3 to 4 % per decade for the 50°C IRSL signal and below 1.5% per decade for the pIRIR₁₇₀ signal. Following (94) the latter is considered negligible and no fading corrections were applied. The resulting pIRIR₁₇₀ ages for Bream Cove and Pendower are stratigraphically consistent, and less scattered than the quartz estimates, both in the sense of the reduced inter-aliquot scatter resulting in greater precision, and also in terms of inter-sample consistency. As such these ages are used as the most likely indicators of site age in all subsequent analyses.

Calculating past local sea level from observations

Indicative ranges for the littoral facies were developed by correlating inferred depositional environments with modern-equivalent formational limits. Global tidal and wave models (95) were used to compute the modern upper and lower formational limits of beach deposits (ordinary berm to breaking depth), estuarine and marine sediments and tidal notches (mean higher high water to mean lower low water). The global tidal and wave models were incapable of accurately computing the elevation of storm wave swash height (SWSH) associated with formational limits of beach ridge (upper formation limit) and foredune (lower formation limit) features (95). Instead, SWSH (defined as the maximum elevation reached by waves during storm events) was estimated

Science Advances Manuscript Template Page 10 of 29

from the elevation of unvegetated beach-ridge crests associated with active modern systems at each site using Google Earth Pro (v. 7.3.3.7786). A similar approach was used to estimate upper formation limits for dune sands by identifying the maximal elevation of vegetated foredune crests. At all relevant sites, vegetated foredune crests tended to occur *c*. 10 m above the elevation of active unvegetated beach ridge crests (i.e., 10 m above SWSH). The upper limit of modern dune sand formation was therefore assigned SWSH +10 m, which provided a conservative upper limit for a one-tailed uncertainty distribution associated with terrestrial-limiting LIG dune sand deposits.

0 The position of former RSL is a function of the elevation of the deposit and the reference water level (RWL) associated with the deposit (96). The RWL for each deposit is taken to be the 2 midpoint of the upper and lower modern formational limit of the deposit (37), with the exception 3 of limiting index points where the RWL is equal to the lower (marine limiting) or upper (terrestrial limiting) modern formational limits of the deposit. For SLIPs, RSL is then equal to the 4 difference of the elevation of the sample (or deposit) and the RWL of the deposit. The range in 5 formational elevation of the modern deposit (i.e., the indicative range) is taken to represent the 2σ 6 vertical uncertainty associated with the sample (or deposit). Here, the elevation for precise SLIPs 7 is taken to be the upper contact of the littoral facies used to determine the indicative range, 8 9 whereas for terrestrial limiting index points (e.g., dune sands) the elevation is taken as the basal contact of the deposit. Uncertainties for SLIPs are root-mean-squared errors of the indicative 0 ranges and a ubiquitous 0.40 m survey error (37) to account for measurement and rounding errors 1 and variability in the elevation of deposit contacts. Uncertainties associated with precise SLIPs 2 are assumed to have Gaussian distributions in both time (x axis) and space (y axis). Changes in 3 the coastline and climate during the LIG (compared to modern) can potentially amplify the tidal 4 range (97) or reduce the storm surge height (98). This uncertainty is acknowledged here, but not 5 added to our data since it is difficult to quantify the appropriate uncertainty that this introduces at 6 our specific locations. 7

Long-term deformation

8

9

Independent from the effects of GIA associated with Late Pleistocene (de)glaciations, the 0 elevation of sea-level indicators such as littoral deposits can alter after deposition due to tectonic 2 crustal deformation, sediment loading (32), and mantle dynamic topography (31). At a passive margin, like our sites, rates associated with these processes are relatively small and constant over 3 the Plio-Pleistocene, but can still add up to several meters since the LIG and therefore need to be 5 4 accounted for. To correct for these collective effects (which we will refer to as 'long-term deformation'), we use site-specific indicators of vertical land motion from outside of the 6 Pleistocene. The majority of our long-term deformation indicators are Pliocene marine rock 7 platforms that are co-located with 24 of the 27 data points in our database. Pliocene marine rock 8 platforms can be found across northern France and southern Britain (c.f., (99-101) and references 9 therein), and often in association with coeval marine littoral deposits (e.g., (99, 102, 103)). Each 0 datapoint in the database is given a Pliocene marine rock platform counterpart (see Supplementay 1 2 Data for additional references): a Pliocene rock platform at an elevation of 130 m ODN extends across parts of Cornwall (104) and Devon (105) and is associated with shallow marine and littoral 3 interbedded sands and clays (104, 106, 107). A synonymous platform at the same elevation is 4 evident across South Wales and has been associated with the Pliocene platforms found on the 5 north coasts of Devon and Cornwall (108, 109). A 120 m ODN marine rock platform on Jersey in 6 the Channel Isles (110, 111) is assigned an analogous age to the 130 m ODN platform in SW 7 Britain by (99). Further east, a Pliocene marine rock platform is extensive across southern Britain 8 and varies in elevation from 100 m ODN (112) to 150 m ODN (113), and is tentatively associated 9 with ~ 150 m of uplift since the Middle Pliocene by (114). In northern France, a recent and 0

extensive mapping of Pliocene platforms and Pleistocene terraces from the Contentin Peninsula (101) has resolved a main Pliocene platform to 138 ± 5 m NFG, whilst correcting for topographic roughness. In the absence of elevation distributions for the platforms described above, we assign an uncertainty of 5 m (1 σ) following (101) as a conservative estimate of the range in elevation to all Pliocene marine rock platforms used in this study.

6 To estimate an uplift rate based on these platform elevations, we first calculate how much 7 GIA affects their elevation and do so following the procedure described in (115) assuming an age 8 range of 3-5 Ma (Supplementary Data). Note that in contrast to (115), we do not use different GMSL histories but instead use the one that best matches their GMSL estimates, which is based on scaling the (116) LR04 oxygen isotope stack. Once corrected for GIA, long-term deformation 0 (in all cases – uplift) is calculated for each datapoint using the GIA-corrected elevation, the age of 1 2 the Pliocene marine rock platforms (3-5 Ma, uniform distribution), and estimate of GMSL (19 \pm 8 m, 1σ , (115)). GMSL was likely highest during the Early Pliocene and therefore best explains the 3 extensive flat marine rock platforms found across parts of Europe. We therefore base our GMSL 4 range on the early Pliocene estimate by (115) who found that GMSL was 10.6–28.3m (16th and 5 84th percentile) above present at 4.39 ± 0.39 (2 σ) Ma. This distribution is further in line with the 6 Pliocene sea level highstands by (117), which average around 16 ± 14 m (1 σ). A distribution of 7 8 uplift rate R at each location is then calculated from the elevation E through:

$$R = (E - GIA - GMSL)/age$$

1

2

3 4

5

9

0

1

2

3

4

5

6

7

8 9

0

2

4

5

6

7

8

9

0

2

3

4

5

6

7

where we sample each individual distribution to propagate uncertainties. The resulting distributions are mostly normal with a slight skew towards lower values. Mean values range from 3.5-4.5 m of uplift since 125 ka with 1σ uncertainties of around 0.7 m. We report the mean and 1σ values for each site in the Supplementary Data and use them in the following inference.

No Plio-Pleistocene platforms or deposits are available as counterparts to the datapoints from Denmark, largely due to Late Cenozoic uplift and erosion of the eastern North Sea Basin (118-120). Late Miocene shallow marine sands that form part of the Oligocene – Miocene sedimentary sequence stratigraphy of Denmark (121) and the wider North Sea region (122) outcrop at the western edge of Denmark at the Marbaek Klint exposure and form part of the upper Miocene Gram Formation (121, 123). These are the youngest deposits that might provide a longterm signal of vertical land motion in Danish onshore stratigraphy. The shallow marine sands of the Marbaek Formation in western Denmark represent a high energy, tidally influenced shoreface environment (121). This formation represents a shallow sea that extended into central Denmark c. 100 m above present-day sea level up until the Late Miocene (121, 124). We are therefore able to estimate a priori long-term uplift rates for data points from Denmark using an elevation of $100 \pm$ 10 m (we conservatively double the uncertainty estimate for this long-term deformation indicator). As for the Pliocene platforms, we correct for GIA assuming a Late Miocene age range of 5-7.5 Ma. We estimate that GMSL was 4 ± 17 m (1σ), which is based on the distribution of GMSL highstands during this time period by (117). Note that GMSL estimates during the Late Miocene by (117) are lower than Pliocene GMSL estimates. The same procedure as described above yields an estimate of uplift since the LIG at this location of 2.43 ± 0.53 m (1σ).

Geologic markers of long-term deformation are absent in York. Since limiting data are not used in our inversion we have not attempted to estimate an uplift correction for this datapoint.

Glacial isostatic adjustment modelling

We employ the gravitationally self-consistent sea level theory described in (41) and (125) to calculate the response of the solid Earth's gravity field, to changes in ice and ocean load. This calculation allows for shoreline migration and includes feedbacks on Earth's rotation axis. In our

Science Advances Manuscript Template Page 12 of 29

GIA calculations we assume that the Earth's elastic structure follows PREM (126) and vary three parameters of the viscous structure: a lithospheric thickness that is either 71 km or 96 km, an upper mantle viscosity that ranges from 0.3 to 0.5 x 10²¹ Pa s, and a lower mantle viscosity that 1 ranges from 3 to 40 x 10²¹ Pa s. Combining these values leads to 48 different models of Earth's 2 viscosity. In addition to the Earth structure, we prescribe the past ice sheet history. We will first describe the ice histories over the glacial cycles used to obtain the glacial GIA-corrected sea level estimates, and then the ice history of Greenland mass loss used to infer the Antarctic sea-level contribution during the LIG.

8

9

3

4

5

7

8 9

0

1 2

3

4 5

6

7

8 9

0

2

3

4 5

6

8

9

0

1

2

3

4

5

6

7

8

9

0

1

2

3

4

5

For the deglaciation we follow the ice history ICE-6G (39). Prior to the last glacial maximum we use the GMSL estimate by (127) back to 400 ka and at each time assign the ice geometry from the deglaciation that corresponds to the same GMSL value. The GMSL during the LIG is set to zero and the GMSL curve prior to the LIG is shifted back by 3.5 ka to result in a PGM age of 135 ka. This ice history from 400 ka to present forms the basis of our GIA calculation. While the ice history over the last deglaciation is relatively well known, there's ample evidence that the ice sheet configuration during the penultimate glacial maximum (and penultimate deglaciation) was significantly different, both in the distribution of ice (29, 40) and timing of ice loss (48). We therefore produce 12 ice models that pair six different ice geometries with two different ice loss timings. For the Eurasian Ice Sheet (EIS) during the penultimate glacial maximum we start with three published ice geometries: ICE-6G (our base model), (29), and (40). Note that the latter two argue for a significantly larger Eurasian ice sheet, which is supported by more extensive terminal moraines during MIS 6 (128). While the sea level equivalent (SLE) ice volume of the EIS during the last glacial maximum is only 23.4 m in ICE-6G, the volume increases to 54m and 70m in the models for the penultimate glacial maximum (PGM) by (29) and (40), respectively (see Fig. S1a, e, f). This increase in ice volume affects LIG sea level around the globe (129, 130). While the GMSL history prior to the PGM is also uncertain (131) its effect on GIA is small compared to uncertainties related to the ice sheet size and distribution (129). To construct a full penultimate glacial cycle, we first use our base ice model and isolate the EIS contribution to GMSL. Since this ice history is based on ICE-6G, the contribution is around 23.4 m during the PGM. Next we scale this GMSL contribution of the EIS up to match the ice volume of the (29) and (40) ice volume. We then use the deglacial GLAC-1D ice history by (132) as our template for EIS collapse. We assume that the last 10 m of EIS contribution come from this ice model. Beyond a GMSL contribution of 10 m, we use a combination of the GLAC-1D ice history (unscaled but fluctuating in accord with the EIS contribution to GMSL) and a scaled version of the selected PGM EIS. The scaling is chosen to obtain a desired EIS contribution to GMSL. The two contributions are combined by taking the maximum ice height between the two at each location. In addition to the three PGM ice configurations mentioned above, we construct 3 additional PGM models that are versions of the (29) ice model that is reduced in size (by scaling its height) to obtain a PGM SLE value for the EIS of 32 m, 40 m, and 47 m (see model LG 32, LG 40, and LG 47 in Fig. S1b-d). The rest of the glacial cycle is constructed as described above.

In all of these scenarios we balance a larger EIS by reducing the size of the Laurentide Ice Sheet. In addition to the GMSL history by (127) we use a slightly modified version during the penultimate glacial cycle with a slower penultimate deglaciation. This earlier onset of the deglaciation is based on a Tahitian coral record (133) (see Fig. S11). The six ice geometries paired with two GMSL scenarios yield 12 different ice histories that are paired with the 48 viscosity structures to produce 576 different GIA models.

This way of constructing the ice sheet leads to a collapse history that we deem relatively realistic in Fennoscandia given that this part of the ice sheet was a major contributor during the penultimate deglaciation. However, the ice sheet is likely too flat towards its south-eastern edge

in many of the models given the simplistic scaling (see Fig. S1g-k). The detailed ice geometry in that region is likely to be less crucial for our data that are located in northwest Europe. In the absence of a range of existing ice sheet models for the penultimate deglaciation we consider that our reconstructions still represent a useful suite of ice histories to test the sensitivity of our glacial GIA models to this input.

1 2

To model the GIA signal associated with melting of the Greenland Ice Sheet over the course of the LIG, we use the same computational model and range of viscosity structures as described above. For the ice history we use eight published Greenland Ice Sheet models for the LIG: the high and low scenario by (43), the IPSL anomaly experiment by (134), the most likely scenario by (44), the three scenarios by (135), and a model based on (136). In each case we linearly interpolate the ice history to 1 ka timesteps over the course of the LIG and only start reducing the ice sheet once the ice volume decreases below present values. The local sea level response in NW Europe is relatively uniform across the region (see Fig. 1a and Fig. S3). Small differences from one place to the next can still exist and those are propagated into the local sea level uncertainty. For each ice model we calculate local sea level by taking the mean and standard deviation across the GIA predictions for each location and each viscosity structure. The resulting local sea level prediction (Fig. 3) we take the mean and standard deviation at each timestep from all data locations, viscosity structures, and ice histories.

Bayesian inversion to infer glacial GIA-corrected sea level

We model LIG glacial GIA-corrected sea level in northern Europe as a Gaussian process, and we fit this Gaussian process to glacial GIA-corrected sea-level data. The mean and covariance components of the Gaussian process are inferred from the paleo-RSL data corrected for each of the 576 potential glacial GIA models using Bayesian inversion. In the inversion model, paleo-RSL data and the associated uncertainty in sample age, elevation, and indicative meaning are treated explicitly as random variables (prior distributions). We estimate the relative probability that each of the 576 glacial GIA models can explain the observations using Bayesian model averaging. Bayesian model averaging provides weights for each of the 576 glacial GIA models, and these weights are used to create a meta-model that combines information learned from each model-data comparison. The next section will describe the details of the inversion model and motivation for those choices.

We remove glacial GIA and long-term uplift from each sea level observation with the following equation (referred to as GIA-corrected sea level):

glacial GIA-corrected sea level = RSL - UPLIFT - GIA

For each index point, RSL is set to a Gaussian distribution with μ = RSL and σ = RSL error.

The uplift and glacial GIA corrections for each observation depend on the age and location of the sample. The ages are treated as Gaussian distributions with μ and σ set to the mean and standard deviation determined from the absolute geochronologies (Supplementary Data). Additionally, the age distributions are bound to the LIG (as defined in our glacial GIA model simulations; 128-117 ky). For each sample of the posterior, ages are drawn from this distribution and then the location-specific glacial GIA correction, using a single glacial GIA model, for that age is applied to the sample. Additionally, an uplift correction is applied to the observation using the posterior age sample and the regional uplift rate.

Science Advances Manuscript Template Page 14 of 29

We then fit a Gaussian process to the set of glacial GIA-corrected sea-level data. The covariance kernel of the Gaussian process is assumed to be the sum of a radial basis function and a white noise kernel. The radial basis function has two parameters that are learned during the inversion: the variance, σ^2 , and the length scale, l. The prior distribution for the length scale is modelled as an inverse Gaussian distribution with $\mu = 2$ and $\lambda = 5$. This length scale effectively ignores changes on short timescales (100s of years) and timescales longer than the LIG (>10 ka). A normal Gaussian distribution with $\mu = 0$ and $\sigma = 5$ is used as a prior for the square root of the variance of the RBF function. A half (positive only) Student T distribution with $v = \text{and } \sigma = 0.1$ is used as a prior for the variance of the white noise kernel. The prior distribution for the mean of the Gaussian process is modelled as a normal Gaussian distribution centred at 0 with a standard deviation of 10.

We sample the posterior distributions with a No U-Turn Sampler (NUTS) using the Python probabilistic programming package PyMC3. The posterior distribution for GIA-corrected sea level was calculated for each glacial GIA model separately. We use leave-one-out crossvalidation (LOO) to determine relative probabilities, or weights, that describe the predictive power of each glacial GIA model (in other words, these weights show how well the model performs at predicting observations that are with-held from model training.) For example, a glacial GIA model that completely removes all spatial variations in the paleo sea-level data should have a relative probability of 1, when compared to a suite of other, less well-fitting models. The weights are then used to create a weighted-mean for glacial GIA-corrected sea level that incorporates all 576 glacial GIA models. One realization of the posterior in this weightedmean meta-model is generated by combining individual posterior realizations from each of the 576 glacial GIA models, sampled at the relative weight of each model. Generally speaking, we continue to generate new realizations of this posterior until the statistics of interest stop changing significantly. In other words, when the posterior mean and variance start to converge, enough realizations have been generated.

References

2

3

4 5

6

7

8

9

0 1

2

3

4 5

6 7

8 9

0

1

2

3

4 5

6

1

2

3

4

5

6

7

8

9

4 5

6

7 8

9

0

1

- A. E. Raftery, A. Zimmer, D. M. W. Frierson, R. Startz, P. Liu, Less Than 2 degrees C 1. Warming by 2100 Unlikely. *Nature Climate Change* 7, 637-641 (2017).
- 2. D. P. van Vuuren, J. Edmonds, M. Kainuma, K. Riahi, A. Thomson, K. Hibbard, G. C. Hurtt, T. Kram, V. Krey, J.-F. Lamarque, T. Masui, M. Meinshausen, N. Nakicenovic, S. J. Smith, S. K. Rose, The representative concentration pathways: an overview. *Climatic* Change 109, 5-31 (2011).
- K. Riahi, D. P. van Vuuren, E. Kriegler, J. Edmonds, B. C. O'Neill, S. Fujimori, N. Bauer, 3. K. Calvin, R. Dellink, O. Fricko, W. Lutz, A. Popp, J. C. Cuaresma, K. C. Samir, M. 0 Leimbach, L. W. Jiang, T. Kram, S. Rao, J. Emmerling, K. Ebi, T. Hasegawa, P. Havlik, F. Humpenoder, L. A. da Silva, S. Smith, E. Stehfest, V. Bosetti, J. Eom, D. Gernaat, T. 1 2 Masui, J. Rogelj, J. Strefler, L. Drouet, V. Krey, G. Luderer, M. Harmsen, K. Takahashi, L. Baumstark, J. C. Doelman, M. Kainuma, Z. Klimont, G. Marangoni, H. Lotze-Campen, 3 M. Obersteiner, A. Tabeau, M. Tavoni, The Shared Socioeconomic Pathways and their energy, land use, and greenhouse gas emissions implications: An overview. Global *Environmental Change-Human and Policy Dimensions* **42**, 153-168 (2017).
 - B. Fox-Kemper, H.T. Hewitt, C. Xiao, G. Aðalgeirsdóttir, S.S. Drijfhout, T.L. Edwards, 4. N.R. Golledge, M. Hemer, R.E. Kopp, G. Krinner, A. Mix, D. Notz, S. Nowicki, I.S. Nurhati, L. Ruiz, J.-B. Sallée, A.B.A. Slangen, Y. Yu, "Ocean, Cryosphere and Sea Level Change." in Climate Change 2021: The Physical Science Basis. Contribution of Working Group I to the Sixth Assessment Report of the Intergovernmental Panel on Climate

- 2 Change, V. Masson-Delmotte, P. Zhai, A. Pirani, S.L. Connors, C. Péan, S. Berger, N.
- Caud, Y. Chen, L. Goldfarb, M.I. Gomis, M. Huang, K. Leitzell, E. Lonnoy, J.B.R.
- Matthews, T.K. Maycock, T. Waterfield, O. Yelekçi, R. Yu, B. Zhou, Eds. (Cambridge University Press, Cambridge, United Kingdom and New York, NY, USA, 2021), pp.
- 6 1211–1362.

- 7 5. R. E. Kopp, R. M. DeConto, D. A. Bader, C. C. Hay, R. M. Horton, S. Kulp, M.
- 8 Oppenheimer, D. Pollard, B. H. Strauss, Evolving Understanding of Antarctic Ice-Sheet
- Physics and Ambiguity in Probabilistic Sea-Level Projections. *Earth's Future* **5**, 1217-1233 (2017).
- 1 6. R. M. DeConto, D. Pollard, R. B. Alley, I. Velicogna, E. Gasson, N. Gomez, S. Sadai, A.
- Condron, D. M. Gilford, E. L. Ashe, R. E. Kopp, D. Li, A. Dutton, The Paris Climate Agreement and future sea-level rise from Antarctica. *Nature* **593**, 83-89 (2021).
- 4 7. T. L. Edwards, S. Nowicki, B. Marzeion, R. Hock, H. Goelzer, H. Seroussi, N. C.
 - Jourdain, D. A. Slater, F. E. Turner, C. J. Smith, C. M. McKenna, E. Simon, A. Abe-
- Ouchi, J. M. Gregory, E. Larour, W. H. Lipscomb, A. J. Payne, A. Shepherd, C. Agosta,
- P. Alexander, T. Albrecht, B. Anderson, X. Asay-Davis, A. Aschwanden, A. Barthel, A.
- 8 Bliss, R. Calov, C. Chambers, N. Champollion, Y. Choi, R. Cullather, J. Cuzzone, C.
- Dumas, D. Felikson, X. Fettweis, K. Fujita, B. K. Galton-Fenzi, R. Gladstone, N. R.
- Golledge, R. Greve, T. Hattermann, M. J. Hoffman, A. Humbert, M. Huss, P. Huybrechts,
- W. Immerzeel, T. Kleiner, P. Kraaijenbrink, S. Le clec'h, V. Lee, G. R. Leguy, C. M.
- Little, D. P. Lowry, J.-H. Malles, D. F. Martin, F. Maussion, M. Morlighem, J. F. O'Neill,
- 3 I. Nias, F. Pattyn, T. Pelle, S. F. Price, A. Quiquet, V. Radić, R. Reese, D. R. Rounce, M.
- 4 Rückamp, A. Sakai, C. Shafer, N.-J. Schlegel, S. Shannon, R. S. Smith, F. Straneo, S. Sun,
- 5 L. Tarasov, L. D. Trusel, J. Van Breedam, R. van de Wal, M. van den Broeke, R.
- 6 Winkelmann, H. Zekollari, C. Zhao, T. Zhang, T. Zwinger, Projected land ice
- 7 contributions to twenty-first-century sea level rise. *Nature* **593**, 74-82 (2021).
- 8 8. M. A. Depoorter, J. L. Bamber, J. A. Griggs, J. T. Lenaerts, S. R. Ligtenberg, M. R. van
- den Broeke, G. Moholdt, Calving fluxes and basal melt rates of Antarctic ice shelves.

 Nature **502**, 89-92 (2013).
- 9. C. Schoof, Ice sheet grounding line dynamics: Steady states, stability, and hysteresis.

 Journal of Geophysical Research 112, (2007).
- 3 10. E. Rignot, S. Jacobs, J. Mouginot, B. Scheuchl, Ice-shelf melting around Antarctica. *Science* **341**, 266-270 (2013).
- 5 11. D. Pollard, R. M. DeConto, R. B. Alley, Potential Antarctic Ice Sheet retreat driven by
- hydrofracturing and ice cliff failure. *Earth and Planetary Science Letters* **412**, 112-121 (2015).
- 8 12. C. Ritz, T. L. Edwards, G. Durand, A. J. Payne, V. Peyaud, R. C. A. Hindmarsh, Potential
- sea-level rise from Antarctic ice-sheet instability constrained by observations. *Nature* **528**, 115-118 (2015).
- 1 13. J. Garbe, T. Albrecht, A. Levermann, J. F. Donges, R. Winkelmann, The hysteresis of the Antarctic Ice Sheet. *Nature* **585**, 538-544 (2020).
- 3 14. J. Hinkel, J. A. Church, J. M. Gregory, E. Lambert, G. Le Cozannet, J. Lowe, K. L.
- McInnes, R. J. Nicholls, T. D. Pol, R. Wal, Meeting User Needs for Sea Level Rise
- Information: A Decision Analysis Perspective. *Earth's Future* **7**, 320-337 (2019).
- 6 15. A. Dutton, A. E. Carlson, A. J. Long, G. A. Milne, P. U. Clark, R. DeConto, B. P. Horton,
- S. Rahmstorf, M. E. Raymo, Sea-level rise due to polar ice-sheet mass loss during past warm periods. *Science* **349**, aaa4019 (2015).
- 9 16. E. Capron, A. Govin, E. J. Stone, V. Masson-Delmotte, S. Mulitza, B. Otto-Bliesner, T. L.
- Rasmussen, L. C. Sime, C. Waelbroeck, E. W. Wolff, Temporal and spatial structure of

Science Advances Manuscript Template Page 16 of 29

- multi-millennial temperature changes at high latitudes during the Last Interglacial. *Quaternary Science Reviews* **103**, 116-133 (2014).
- M.-V. Guarino, L. C. Sime, D. Schröeder, I. Malmierca-Vallet, E. Rosenblum, M. Ringer, J. Ridley, D. Feltham, C. Bitz, E. J. Steig, E. Wolff, J. Stroeve, A. Sellar, Sea-ice-free Arctic during the Last Interglacial supports fast future loss. *Nature Climate Change* **10**, 928-932 (2020).
- 7 18. T. L. Edwards, M. A. Brandon, G. Durand, N. R. Edwards, N. R. Golledge, P. B. Holden, I. J. Nias, A. J. Payne, C. Ritz, A. Wernecke, Revisiting Antarctic ice loss due to marine ice-cliff instability. *Nature* **566**, 58-64 (2019).
- 1 R. M. DeConto, D. Pollard, Contribution of Antarctica to past and future sea-level rise.

 Nature **531**, 591-597 (2016).
- 2 20. R. E. Kopp, F. J. Simons, J. X. Mitrovica, A. C. Maloof, M. Oppenheimer, Probabilistic assessment of sea level during the last interglacial stage. *Nature* **462**, 863-867 (2009).
- 4 21. B. Dyer, J. Austermann, W. J. D'Andrea, R. C. Creel, M. R. Sandstrom, M. Cashman, A. Rovere, M. E. Raymo, Sea-level trends across The Bahamas constrain peak last interglacial ice melt. *Proc Natl Acad Sci U S A* 118, (2021).
- A. Dutton, J. M. Webster, D. Zwartz, K. Lambeck, B. Wohlfarth, Tropical tales of polar ice: evidence of Last Interglacial polar ice sheet retreat recorded by fossil reefs of the granitic Seychelles islands. *Quaternary Science Reviews* **107**, 182-196 (2015).
- E. J. Rohling, F. D. Hibbert, K. M. Grant, E. V. Galaasen, N. Irvalı, H. F. Kleiven, G.
 Marino, U. Ninnemann, A. P. Roberts, Y. Rosenthal, H. Schulz, F. H. Williams, J. Yu,
 Asynchronous Antarctic and Greenland ice-volume contributions to the last interglacial
 sea-level highstand. *Nature Communications* 10, 5040 (2019).
- 4 24. M. J. O'Leary, P. J. Hearty, W. G. Thompson, M. E. Raymo, J. X. Mitrovica, J. M. Webster, Ice sheet collapse following a prolonged period of stable sea level during the last interglacial. *Nature Geoscience* **6**, 796-800 (2013).
- N. L. M. Barlow, E. L. McClymont, P. L. Whitehouse, C. R. Stokes, S. S. R. Jamieson, S. A. Woodroffe, M. J. Bentley, S. L. Callard, C. Ó. Cofaigh, D. J. A. Evans, J. R. Horrocks, J. M. Lloyd, A. J. Long, M. Margold, D. H. Roberts, M. L. Sanchez-Montes, Lack of evidence for a substantial sea-level fluctuation within the Last Interglacial. *Nature Geoscience* 11, 627-634 (2018).
- 2 26. C. Hay, J. X. Mitrovica, N. Gomez, J. R. Creveling, J. Austermann, R. E. Kopp, The sealevel fingerprints of ice-sheet collapse during interglacial periods. *Quaternary Science* 4 *Reviews* 87, 60-69 (2014).
- 5 27. D. M. Gilford, E. L. Ashe, R. M. DeConto, R. E. Kopp, D. Pollard, A. Rovere, Could the 6 Last Interglacial Constrain Projections of Future Antarctic Ice Mass Loss and Sea-Level 7 Rise? *Journal of Geophysical Research: Earth Surface* 125, (2020).
- 8 28. A. J. Long, N. L. M. Barlow, F. S. Busschers, K. M. Cohen, W. R. Gehrels, L. M. Wake, 9 Near-field sea-level variability in northwest Europe and ice sheet stability during the last 0 interglacial. *Quaternary Science Reviews* 126, 26-40 (2015).
- 1 29. K. Lambeck, A. Purcell, S. Funder, K. H. KjaeR, E. Larsen, P. E. R. Moller, Constraints on the Late Saalian to early Middle Weichselian ice sheet of Eurasia from field data and rebound modelling. *Boreas* 35, 539-575 (2006).
- 4 30. K. Lambeck, A. Purcell, A. Dutton, The anatomy of interglacial sea levels: The relationship between sea levels and ice volumes during the Last Interglacial. *Earth and Planetary Science Letters* **315-316**, 4-11 (2012).
- J. Austermann, J. X. Mitrovica, P. Huybers, A. Rovere, Detection of a dynamic topography signal in last interglacial sea-level records. *Sci Adv* 3, e1700457 (2017).

Science Advances Manuscript Template Page 17 of 29

- A. R. Simms, J. B. Anderson, R. DeWitt, K. Lambeck, A. Purcell, Quantifying rates of coastal subsidence since the last interglacial and the role of sediment loading. *Global and Planetary Change* **111**, 296-308 (2013).
- 2 33. Y. Zhou, J. McManus, Extensive evidence for a last interglacial Laurentide outburst (LILO) event. *Geology* **50**, 934-938 (2022).
- 4 34. H. T. de la Beche, *The geology of Cornwall and Devon and part of W. Somerset* (Memoirs of the Ordnance Geological Survey, London, 1839).
- 6 35. S. Campbell, C. O. Hunt, J. D. Scourse, D. H. Keen, D. G. Croot, "Southwest England" in
 A revised correlation of Quaternary deposits in the British Isles (Geological Society of
 London, 1999), vol. 23, chap. 6, pp. 66-78.
- 9 36. S. Campbell, C. O. Hunt, J. D. Scourse, D. H. Keen, N. Stephens, *Quaternary of South-West England* (Geological Conservation Review Series Springer Dordrecht, 1998).
 - 37. A. Rovere, M. E. Raymo, M. Vacchi, T. Lorscheid, P. Stocchi, L. Gómez-Pujol, D. L.
- Harris, E. Casella, M. J. O'Leary, P. J. Hearty, The analysis of Last Interglacial (MIS 5e) relative sea-level indicators: Reconstructing sea-level in a warmer world. *Earth-Science Reviews* **159**, 404-427 (2016).
- 5 38. K. M. Cohen, V. Cartelle, R. Barnett, F. S. Busschers, N. L. M. Barlow, Last Interglacial sea-level data points from Northwest Europe. *Earth System Science Data* **14**, 2895-2937 (2022).
- W. R. Peltier, D. F. Argus, R. Drummond, Space geodesy constrains ice age terminal deglaciation: The global ICE-6G_C (VM5a) model. *Journal of Geophysical Research:*Solid Earth 120, 450-487 (2015).
- 1 40. F. Colleoni, C. Wekerle, J.-O. Näslund, J. Brandefelt, S. Masina, Constraint on the penultimate glacial maximum Northern Hemisphere ice topography (≈140 kyrs BP).

 3 Ouaternary Science Reviews 137, 97-112 (2016).
- 4 41. R. A. Kendall, J. X. Mitrovica, G. A. Milne, On post-glacial sea level II. Numerical formulation and comparative results on spherically symmetric models. *Geophysical Journal International* **161**, 679-706 (2005).
- O. G. Pollard, N. L. M. Barlow, L. Gregoire, N. Gomez, V. Cartelle, J. C. Ely, L. C. Astfalck, Quantifying the Uncertainty in the Eurasian Ice-Sheet Geometry at the Penultimate Glacial Maximum (Marine Isotope Stage 6). *The Cryosphere Discuss*. [preprint], (in review, 2023).
- R. Calov, A. Robinson, M. Perrette, A. Ganopolski, Simulating the Greenland ice sheet under present-day and palaeo constraints including a new discharge parameterization. *The Cryosphere* **9**, 179-196 (2015).
- 4 44. A. M. Yau, M. L. Bender, A. Robinson, E. J. Brook, Reconstructing the last interglacial at Summit, Greenland: Insights from GISP2. *Proc Natl Acad Sci U S A* **113**, 9710-9715 (2016).
- J. S. Hoffman, P. U. Clark, A. C. Parnell, F. He, Regional and global sea-surface temperatures during the last interglaciation. *Science* **355**, 276-279 (2017).
- D. Farinotti, M. Huss, J. J. Fürst, J. Landmann, H. Machguth, F. Maussion, A. Pandit, A consensus estimate for the ice thickness distribution of all glaciers on Earth. *Nature Geoscience* **12**, 168-173 (2019).
- 2 47. N. R. Golledge, P. U. Clark, F. He, A. Dutton, C. S. M. Turney, C. J. Fogwill, T. R. Naish,
- R. H. Levy, R. M. McKay, D. P. Lowry, N. A. N. Bertler, G. B. Dunbar, A. E. Carlson, Retreat of the Antarctic Ice Sheet During the Last Interglaciation and Implications for
- 5 Future Change. *Geophysical Research Letters* **48**, (2021).
- P. U. Clark, F. He, N. R. Golledge, J. X. Mitrovica, A. Dutton, J. S. Hoffman, S. Dendy, Oceanic forcing of penultimate deglacial and last interglacial sea-level rise. *Nature* **577**,

660-664 (2020).

8

1

Science Advances Manuscript Template Page 18 of 29

- 9 49. S. Sun, F. Pattyn, E. G. Simon, T. Albrecht, S. Cornford, R. Calov, C. Dumas, F. Gillet-Chaulet, H. Goelzer, N. R. Golledge, R. Greve, M. J. Hoffman, A. Humbert, E. 0
- Kazmierczak, T. Kleiner, G. R. Leguy, W. H. Lipscomb, D. Martin, M. Morlighem, S. 1
- Nowicki, D. Pollard, S. Price, A. Quiquet, H. Seroussi, T. Schlemm, J. Sutter, R. S. W. 2
- van de Wal, R. Winkelmann, T. Zhang, Antarctic ice sheet response to sudden and 3 sustained ice-shelf collapse (ABUMIP). Journal of Glaciology 66, 891-904 (2020). 4
- 5 50. C. S. M. Turney, C. J. Fogwill, N. R. Golledge, N. P. McKay, E. van Sebille, R. T. Jones,
- D. Etheridge, M. Rubino, D. P. Thornton, S. M. Davies, C. B. Ramsey, Z. A. Thomas, M. 6 I. Bird, N. C. Munksgaard, M. Kohno, J. Woodward, K. Winter, L. S. Weyrich, C. M. 7
 - Rootes, H. Millman, P. G. Albert, A. Rivera, T. van Ommen, M. Curran, A. Moy, S.
- Rahmstorf, K. Kawamura, C. D. Hillenbrand, M. E. Weber, C. J. Manning, J. Young, A. 9
- Cooper, Early Last Interglacial ocean warming drove substantial ice mass loss from 0 Antarctica. *Proc Natl Acad Sci U S A* **117**, 3996-4006 (2020). 1
- A. S. Hein, J. Woodward, S. M. Marrero, S. A. Dunning, E. J. Steig, S. P. Freeman, F. M. 2 51.
- Stuart, K. Winter, M. J. Westoby, D. E. Sugden, Evidence for the stability of the West 3 4 Antarctic Ice Sheet divide for 1.4 million years. Nat Commun 7, 10325 (2016).
- 5 52. L. Pan, E. M. Powell, K. Latychev, J. X. Mitrovica, J. R. Creveling, N. Gomez, M. J.
- Hoggard, P. U. Clark, Rapid postglacial rebound amplifies global sea level rise following 6 7 West Antarctic Ice Sheet collapse. Sci Adv 7, (2021).
- E. M. Powell, L. Pan, M. J. Hoggard, K. Latychev, N. Gomez, J. Austermann, J. X. 8 53.
- Mitrovica, The impact of 3-D Earth structure on far-field sea level following interglacial 9 0 West Antarctic Ice Sheet collapse. *Quaternary Science Reviews* **273**, (2021).
- PAGES (Past Interglacial Working Group of Past Global Changes), Interglacials of the 54. 1 last 800,000 years. Reviews of Geophysics 54, 162-219 (2016). 2
- 3 55. J. D. Scourse, Late Pleistocene Stratigraphy of North and West Cornwall. *Transactions* Royal Geological Society Cornwall 22, 2-56 (1996). 4
- 5 H. L. James, Raised beaches of West Cornwall and their evolving chronology. 56. 6
- *Proceedings of the Ussher Society* **8**, 437-440 (1995).

- H. C. L. James, Aspects of the raised beaches of South Cornwall. Proceedings of the 7 57. *Ussher Society* **2**, 55-56 (1968). 8
- H. C. L. James, Pleistocene sections as Gerrans Bay, south Cornwall. Proceedings of the 9 58. *Ussher Society* **5**, 238 (1981). 0
- 59. G. A. T. Duller, Luminescence dating: Guidelines on using luminescence dating in 1 2 archaeology (English Heritage, Swindon, 2008).
- G. Masselink, T. Scott, T. Poate, P. Russell, M. Davidson, D. Conley, The extreme 3 60. 2013/2014 winter storms: hydrodynamic forcing and coastal response along the southwest 4 coast of England. Earth Surface Processes and Landforms 41, 378-391 (2015). 5
- B. E. H. Leveridge, M.T.; Goode, A.J.J.; Scrivener, R.C.; Monkhouse, R.A.; British 61. 6 Geological Survey., Geology of the country around Falmouth: memoir for the 1:50 000
- 7 8 geological sheet 352 (England & Wales) (Memoirs of the Geological Survey of Great Britain, England and Wales (Sheet - New Series), HMSO, London, 1990). 9
- H. C. L. James, The coastal palaeo-morphology of West Cornwall with particular 0 62.
- reference to shore (wave-cut) platforms. . Transactions of the Royal Geological Society of 1 Cornwall 22, 121-144 (2003). 2
- 3 M. D. Bateman, J. A. Catt, An absolute chronology for the raised beach and associated 63.
- 4 deposits at Sewerby, East Yorkshire, England. Journal of Quaternary Science 11, 389-395 5
- 6 64. A. G. Wintle, Luminescence dating: laboratory procedures and protocols. *Radiation* 7 Measurements 27, 769-817 (1997).
- M. J. Aitken, *Thermoluminescence dating* (Academic Press, London, 1985). 65.

Manuscript Template Page 19 of 29 Science Advances

- 9 66. M. J. Aitken, An Introduction to Optical Dating. The Dating of Quaternary Sediments by 0 the Use of Photon-Stimulated Luminescence (Oxford University Press, Oxford, New York, 1 Tokyo, 1998).
- 2 67. G. Guerin, Mercier, N., Adamiec, G., Dose-rate conversion factors: update. *Ancient TL* **29**, 5-8 (2011).
- 4 68. S. Balescu, M. Lamothe, Thermoluminescence dating of the holsteinian marine formation of Herzeele, northern France. *Journal of Quaternary Science* **8**, 117-124 (1993).
- 6 69. D. J. Huntley, Baril D.J., The K content of the K-feldspars being measured in optical dating or in thermoluminescence dating. *Ancient TL* **15**, 11-13 (1997).
- D. J. Huntley, Hancock, R.G.V., The Rb contents of the K-feldspars being measured in optical dating. *Ancient TL* **19**, 43–46 (2001).
- J. R. Prescott, J. T. Hutton, Cosmic ray contributions to dose rates for luminescence and ESR dating: Large depths and long-term time variations. *Radiation Measurements* **23**, 497-500 (1994).
- A. S. Murray, A. G. Wintle, Luminescence dating of quartz using an improved single-aliquot regenerative-dose protocol. *Radiation Measurements* **32**, 57-73 (2000).
- A. S. Murray, A. G. Wintle, The single aliquot regenerative dose protocol: potential for improvements in reliability. *Radiation Measurements* **37**, 377-381 (2003).
- 7 74. G. A. T. Duller, Assessing the error on equivalent dose estimates derived from single aliquot regenerative dose measurements. *Ancient TL* **25**, 15-24 (2007).
- 9 75. A. C. Cunningham, J. Wallinga, Selection of integration time intervals for quartz OSL decay curves. *Quaternary Geochronology* **5**, 657-666 (2010).
- 1 76. S. J. Armitage, R. M. Bailey, The measured dependence of laboratory beta dose rates on sample grain size. *Radiation Measurements* **39**, 123-127 (2005).
- 77. R. F. Galbraith, R. G. Roberts, G. M. Laslett, H. Yoshida, J. M. Olley, Optical Dating of Single and Multiple Grains of Quartz from Jinmium Rock Shelter, Northern Australia: Part I, Experimental Design and Statistical Models. *Archaeometry* 41, 339-364 (1999).
- 6 78. K. J. Thomsen, A. S. Murray, M. Jain, L. Bøtter-Jensen, Laboratory fading rates of various luminescence signals from feldspar-rich sediment extracts. *Radiation Measurements* **43**, 1474-1486 (2008).
- 9 79. J. P. Buylaert, A. S. Murray, K. J. Thomsen, M. Jain, Testing the potential of an elevated temperature IRSL signal from K-feldspar. *Radiation Measurements* **44**, 560-565 (2009).
- 1 80. A. G. Wintle, Anomalous Fading of Thermo-luminescence in Mineral Samples. *Nature* 2 245, 143-144 (1973).
- 3 81. D. J. Huntley, M. Lamothe, Ubiquity of anomalous fading in K-feldspars and the measurement and correction for it in optical dating. *Canadian Journal of Earth Sciences* 38, 1093-1106 (2001).
- 6 82. M. Jain, J. P. Buylaert, K. J. Thomsen, A. S. Murray, Further investigations on 'non-fading' in K-Feldspar. *Quaternary International* **362**, 3-7 (2015).
- 8 83. J. Wallinga, A. Murray, A. Wintle, The single-aliquot regenerative-dose (SAR) protocol applied to coarse-grain feldspar. *Radiation Measurements* **32**, 529-533 (2000).
- A. S. Murray, J. I. Svendsen, J. Mangerud, V. I. Astakhov, Testing the accuracy of quartz OSL dating using a known-age Eemian site on the river Sula, northern Russia. *Quaternary Geochronology* 2, 102-109 (2007).
- M. S. Chapot, H. M. Roberts, G. A. T. Duller, Z. P. Lai, A comparison of natural- and laboratory-generated dose response curves for quartz optically stimulated luminescence signals from Chinese Loess. *Radiation Measurements* **47**, 1045-1052 (2012).
- 5 J. Peng, X. Wang, G. Adamiec, The build-up of the laboratory-generated dose-response curve and underestimation of equivalent dose for quartz OSL in the high dose region: A critical modelling study. *Quaternary Geochronology* **67**, (2022).

Science Advances Manuscript Template Page 20 of 29

- 9 87. A. Murray, J.-P. Buylaert, M. Henriksen, J.-I. Svendsen, J. Mangerud, Testing the reliability of quartz OSL ages beyond the Eemian. *Radiation Measurements* **43**, 776-780 (2008).
- S. M. Pawley, P. Toms, S. J. Armitage, J. Rose, Quartz luminescence dating of Anglian Stage (MIS 12) fluvial sediments: Comparison of SAR age estimates to the terrace chronology of the Middle Thames valley, UK. *Quaternary Geochronology* 5, 569-582 (2010).
- 6 89. A. G. Wintle, A. S. Murray, A review of quartz optically stimulated luminescence characteristics and their relevance in single-aliquot regeneration dating protocols. *Radiation Measurements* **41**, 369-391 (2006).
- 9 90. A. Madsen, J.-P. Buylaert, A. Murray, Luminescence dating of young coastal deposits from New Zealand using feldspar. *Geochronometria* **38**, 379-390 (2011).
- 1 91. E. F. Rades, S. Tsukamoto, M. Frechen, Q. Xu, L. Ding, A lake-level chronology based on feldspar luminescence dating of beach ridges at Tangra Yum Co (Southern Tibet).

 2 Quaternary Research 83, 469-478 (2017).
- 92. C. J. Oldknow, A. S. Carr, J. M. Hooke, Z. Shen, The suitability of a low temperature
 post-IR IRSL signal for dating alluvial and colluvial "cut and fill" sequences in the Great
 Karoo, South Africa. *Quaternary Geochronology* 58, (2020).
- M. Auclair, M. Lamothe, S. Huot, Measurement of anomalous fading for feldspar IRSL using SAR. *Radiation Measurements* **37**, 487-492 (2003).
- 9 94. J.-P. Buylaert, M. Jain, A. S. Murray, K. J. Thomsen, C. Thiel, R. Sohbati, A robust feldspar luminescence dating method for Middle and Late Pleistocene sediments. *Boreas* 41, 435-451 (2012).
- T. Lorscheid, A. Rovere, The indicative meaning calculator quantification of paleo sealevel relationships by using global wave and tide datasets. *Open Geospatial Data*, *Software and Standards* **4**, 10 (2019).
- 5 96. I. Shennan, Long, A.J., Horton, B.P., "Handbook of sea-level research: framing research questions" in *Handbook of Sea-Level Research*, I. Shennan, Long, A.J., Horton, B.P., Ed. (Wiley, UK, 2015), pp. 3-28.
- T. Lorscheid, T. Felis, P. Stocchi, J. C. Obert, D. Scholz, A. Rovere, Tides in the Last Interglacial: insights from notch geometry and palaeo tidal models in Bonaire, Netherland Antilles. *Sci Rep* 7, 16241 (2017).
- 98. P. Scussolini, J. Dullaart, S. Muis, A. Rovere, P. Bakker, D. Coumou, H. Renssen, P. J. Ward, J. C. J. H. Aerts, Modeled storm surge changes in a warmer world: the Last Interglacial. *Climate of the Past* 19, 141-157 (2023).
- 4 99. R. Westaway, Cenozoic uplift of southwest England. *Journal of Quaternary Science* **25**, 419-432 (2010).
- 6 100. J. R. Lee, Candy, I., Haslam, R., The Neogene and Quaternary of England: landscape evolution, tectonics, climate change and their expression in the geological record. .

 8 Proceedings of the Geologist's Association 129, 452-481 (2018).
- K. Pedoja, J. Jara-Muñoz, G. De Gelder, J. Robertson, M. Meschis, D. Fernandez-Blanco,
 M. Nexer, Y. Poprawski, O. Dugué, B. Delcaillau, P. Bessin, M. Benabdelouahed, C.
 Authemayou, L. Husson, V. Regard, D. Menier, B. Pinel, Neogene-Quaternary slow
 coastal uplift of Western Europe through the perspective of sequences of strandlines from
 the Cotentin Peninsula (Normandy, France). Geomorphology 303, 338-356 (2018).
- the Cotentin Peninsula (Normandy, France). *Geomorphology* **303**, 338-356 (2018).

 J.-P. Lautridou, Baize, S., Clet, M., Coutard, J.-P., Ozouf, J.-C., Littoral and estuarine Plio-Pleistocene sequences in Normandy (France). *Quaternaire* **10**, 161-169 (1999).
- 6 103. O. Dugué, The Pliocene to Early Pleistocene marine to fluviatile succession of the Seuil du Cotentin basins (Armorican Massif, Normandy, France). *Journal of Quaternary Science* **18**, 215-226 (2003).

Science Advances Manuscript Template Page 21 of 29

- 9 104. J. Robson, The recent geology of Cornwall. *Transactions of the Royal Geological Society* of Cornwall **17**, 132-163 (1944).
- 1 105. D. Brunsden, The erosion surfaces of the River Dart. *Proceedings of the Ussher Society*, 35-36 (1962).
- B. Coque-Delhuille, "Le massif du Sud-ouest Anglais et sa bordure sédimentaire; étude géomorphologique", thesis, Université de Paris Panthenon Sorbonne (1987).
- H. B. Milner, The Nature and Origin of the Pliocene Deposits of the County of Cornwall, and their Bearing on the Pliocene Geography of the South-West of England. *Quarterly Journal of the Geological Society* **78**, 348-377 (1922).
- 8 108. A. A. Miller, The 600-Foot Plateau in Pembrokeshire and Carmarthenshire. *The Geographical Journal* **90**, 148-159 (1937).
- 0 109. W. G. V. Balchin, The Erosion Surfaces of Exmoor and Adjacent Areas. *The Geographical Journal* **118**, (1952).
- 2 110. A. C. Bishop, in *Classic areas of British Geology, London*. (British Geological Service, 1989).
- D. H. Keen, "Pre-Flandrian Quaternary deposits, landforms and environments" in *The Quaternary of Jersey. Quaternary Research Association Field Guide*, D. H. Keen, Ed. (London, 1993).
- 7 112. J. F. N. Green. (Proceedings of the Geologists' Association, 1946), vol. 57(2), pp. 82-101.
- 8 113. C. E. Everard, Erosion Platforms on the Borders of the Hampshire Basin. *Transactions of the Institute of British Geographers* **22**, 33-46 (1956).
- R. Westaway, D. Bridgland, M. White, The Quaternary uplift history of central southern England: evidence from the terraces of the Solent River system and nearby raised beaches. Quaternary Science Reviews 25, 2212-2250 (2006).
- 3 115. O. A. Dumitru, J. Austermann, V. J. Polyak, J. J. Fornos, Y. Asmerom, J. Gines, A. Gines, B. P. Onac, Constraints on global mean sea level during Pliocene warmth. *Nature* **574**, 233-236 (2019).
- L. E. Lisiecki, M. E. Raymo, A Pliocene-Pleistocene stack of 57 globally distributed
 benthic δ18O records. *Paleoceanography* 20, n/a-n/a (2005).
- 8 117. K. G. Miller, J. V. Browning, W. J. Schmelz, R. E. Kopp, G. S. Mountain, J. D. Wright,
 9 Cenozoic sea-level and cryospheric evolution from deep-sea geochemical and continental
 0 margin records. *Sci Adv* 6, eaaz1346 (2020).
- 1 118. P. Japsen, T. Bidstrup, E. S. Rasmussen, Comment on: "Cenozoic evolution of the eastern Danish North Sea" by M. Huuse, H. Lykke-Andersen and O. Michelsen, [Marine Geology 177, 243–269]. *Marine Geology* 186, 571-575 (2002).
- 4 119. M. Huuse, H. Lykke-Andersen, O. Michelsen, Cenozoic evolution of the eastern Danish North Sea. *Marine Geology* **177**, 243-269 (2001).
- 6 120. M. Huuse, Late Cenozoic palaeogeography of the eastern North Sea Basin: climatic vs 7 tectonic forcing of basin margin uplift and deltaic progradation. *Bulletin of the Geological* 8 *Society of Denmark* **49**, 145-170 (2002).
- 9 121. E. S. Rasmussen, K. Dybkjær, S. Piasecki, Lithostratigraphy of the Upper Oligocene –
 0 Miocene succession of Denmark. *Geological Survey of Denmark and Greenland Bulletin*1 **22**, 1-92 (2010).
- T. Eidvin, F. Riis, E. S. Rasmussen, Oligocene to Lower Pliocene deposits of the Norwegian continental shelf, Norwegian Sea, Svalbard, Denmark and their relation to the uplift of Fennoscandia: A synthesis. *Marine and Petroleum Geology* **56**, 184-221 (2014).
- 5 123. S. Piasecki, Rasmussen, E.S., Dybkjaer, K., "Neogene sedimenter ved Sjaelborg og Marrebaek Klint, Esberg, Vest-jylland" (2002).

Science Advances Manuscript Template Page 22 of 29

- E. S. Rasmussen, Stratigraphy and depositional evolution of the uppermost Oligocene Miocene succession in western Denmark. *Bulletin of the Geological Society of Denmark* **51**, 89-109 (2004).
- 125. A. V. Dalca, K. L. Ferrier, J. X. Mitrovica, J. T. Perron, G. A. Milne, J. R. Creveling, On postglacial sea level—III. Incorporating sediment redistribution. *Geophysical Journal International* **194**, 45-60 (2013).
- 3 126. A. M. Dziewonski, D. L. Anderson, Preliminary reference Earth model. *Physics of the Earth and Planetary Interiors* **25**, 297-356 (1981).
- 5 127. C. Waelbroeck, L. Labeyrie, E. Michel, J. C. Duplessy, J. F. McManus, K. Lambeck, E. Balbon, M. Labracherie, Sea-level and deep water temperature changes derived from benthic foraminifera isotopic records. *Quaternary Science Reviews* 21, 295-305 (2002).
- 8 128. C. L. Batchelor, M. Margold, M. Krapp, D. K. Murton, A. S. Dalton, P. L. Gibbard, C. R. Stokes, J. B. Murton, A. Manica, The configuration of Northern Hemisphere ice sheets through the Quaternary. *Nature Communications* **10**, 3713 (2019).
- 1 129. S. Dendy, J. Austermann, J. R. Creveling, J. X. Mitrovica, Sensitivity of Last Interglacial sea-level high stands to ice sheet configuration during Marine Isotope Stage 6. *Quaternary Science Reviews* 171, 234-244 (2017).
- E. J. Rohling, F. D. Hibbert, F. H. Williams, K. M. Grant, G. Marino, G. L. Foster, R.
 Hennekam, G. J. de Lange, A. P. Roberts, J. Yu, J. M. Webster, Y. Yokoyama,
 Differences between the last two glacial maxima and implications for ice-sheet, δ18O, and
 sea-level reconstructions. *Quaternary Science Reviews* 176, 1-28 (2017).
- J. D. Shakun, D. W. Lea, L. E. Lisiecki, M. E. Raymo, An 800-kyr record of global surface ocean δ18O and implications for ice volume-temperature coupling. *Earth and Planetary Science Letters* 426, 58-68 (2015).
- 1 132. L. Tarasov, Hughes, A., Gyllencreutz, R., Lohne, O.S., Mangerud, J., Svendsen, J.I., paper presented at the IGS Symposium on Contribution of Glaciers and Ice Sheets to Sea-Level Change, 2014.
- 4 133. A. L. Thomas, G. M. Henderson, P. Deschamps, Y. Yokoyama, A. J. Mason, E. Bard, B. Hamelin, N. Durand, G. Camoin, Penultimate deglacial sea-level timing from uranium/thorium dating of Tahitian corals. *Science* **324**, 1186-1189 (2009).
- A. Quiquet, C. Ritz, H. J. Punge, D. Salas y Mélia, Greenland ice sheet contribution to sea level rise during the last interglacial period: a modelling study driven and constrained by ice core data. *Climate of the Past* **9**, 353-366 (2013).
- 1 H. Goelzer, P. Huybrechts, M.-F. Loutre, T. Fichefet, Last Interglacial climate and sealevel evolution from a coupled ice sheet–climate model. *Climate of the Past* 12, 2195-2213 (2016).
- 3 136. S. L. Bradley, T. J. Reerink, R. S. W. van de Wal, M. M. Helsen, Simulation of the Greenland Ice Sheet over two glacial-interglacial cycles: investigating a sub-ice-shelf melt parameterization and relative sea level forcing in an ice-sheet-ice-shelf model. *Climate of the Past* 14, 619-635 (2018).

Acknowledgments

7 8 9

0

1

2

4

5 6 The authors acknowledge PALSEA, a working group of the International Union for Quaternary Sciences (INQUA) and Past Global Changes (PAGES), which in turn received support from the Swiss Academy of Sciences and the Chinese Academy of Sciences. Special thanks go to Prof. Dan Charman (University of Exeter) for commenting on an early draft of the manuscript and for career mentorship to RLB. We thank three anonymous reviewers for their detailed and constructive feedback.

Science Advances Manuscript Template Page 23 of 29

| 7 | Funding: RLB acknowledges a Research Fellowship from the University of Exeter and |
|--------|---|
| 8 | funding from the Sécurité publique du Québec to the University of Quebec at Rimouski. |
| 9 | JA, BD, and RC acknowledge funding from NSF grant OCE-1841888. JA acknowledges |
| 0 1 | support from the Vetlesen Foundation. NLMB received support for this work from European Research Council (ERC) under the European Union's Horizon 2020 research |
| 2 | and innovation programme (RISeR, grant agreement no. 802281). MWT and SJB received |
| 3 | funding for fieldwork from the University of Plymouth's Marine Institute. |
| 4 | |
| 5 | Author contributions: |
| 6 | Conceptualization: RLB, JA, BD, MT, RC, NLMB |
| 7 | Methodology: RLB, JA, BD, RC |
| 8 | Software: JA, BD |
| 9 | Validation: JA, BD |
| 0 | Formal Analysis: JA, BD, MT |
| 1 | Investigation: ASC, SB, MT, RC |
| 2 | Resources: ASC |
| 3 | Data Curation: RLB |
| 4 | Visualization: RLB, JA, BD, RC |
| 5 | Supervision: NLMB |
| 6 | Writing—original draft: RLB, JA, BD |
| 7 | Writing—review & editing: RLB, JA, BD, ASC, SB, MT, RC, NLMB |
| 8 | Funding acquisition: MT, SB, NLMB, JA |
| 9 | |
| 0 | Competing interests: Authors declare that they have no competing interests. |
| 1 2 | Competing interests. Authors declare that they have no competing interests. |
| 3 | Data and materials availability: The Bayesian inversion code is available on GitHub |
| 4 | (https://github.com/blakedyer/bahamas_lig/). The GIA code is also available on GitHub |
| 5 | (https://github.com/jaustermann/SLcode). All sea level and OSL data are available in the |
| 6 7 | main text or the supplementary materials. |

Science Advances Manuscript Template Page 24 of 29

Figures and Tables

8 9

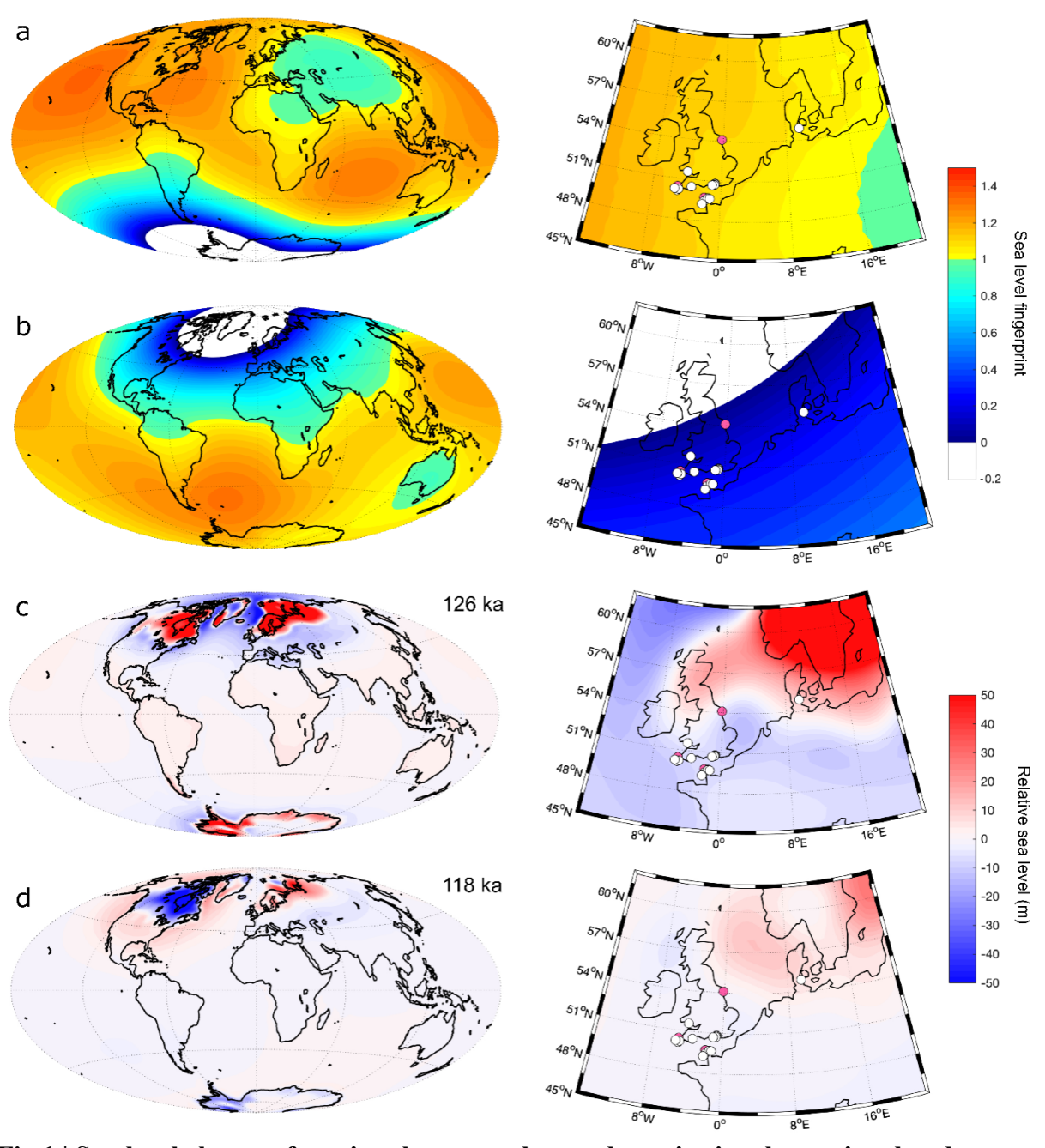


Fig.1 | **Sea-level changes from ice-sheet mass loss and gravitational, rotational and deformational effects. a.** Normalized global (left panel) and regional (NW Europe, right panel) sea-level changes from instantaneous West Antarctic Ice Sheet mass loss (following (26)). The scale is normalized to 1 and demonstrates the sensitivity of NW Europe to WAIS mass loss. White and pink markers denote the location of sea-level index points and sea-level limiting data, respectively. **b.** Normalized global and regional sea-level changes caused by instantaneous mass loss from the Greenland Ice Sheet following the ice melt pattern in (43); white regions are areas of sea-level fall. This demonstrates the general insensitivity of sea level in NW Europe to GIS mass loss. **c.** Relative sea-level changes due to GIA at 126 ka based on a well performing GIA model (i.e., 71 km lithosphere thickness, upper and lower mantle viscosities of 0.5×10^{21} Pa s and 5×10^{21} Pa s, respectively, a Eurasian Ice Sheet with an ice mass sea-level equivalent of 40 m, and a 'slow' deglaciation rate, see Fig. S1g-k). **d.** Same as for **c.** but at 118 ka.

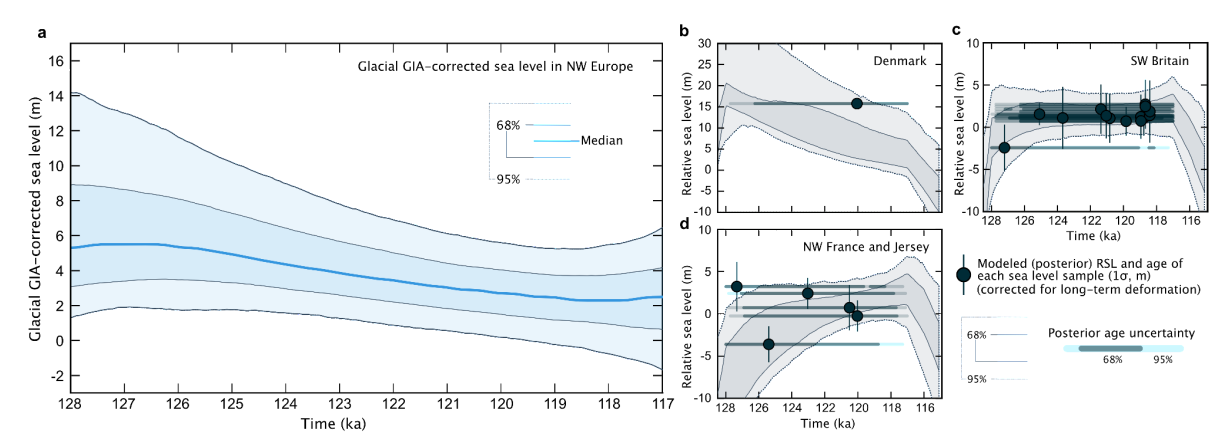


Fig. 2 | Last Interglacial sea-level highstand in NW Europe. a. Estimated last interglacial sea level in NW Europe after accounting for long-term deformation and glacial GIA, showing the median (solid blue line) posterior estimate of the Bayesian inversion along with the central 68% (grey shading) and 95% (light-grey shading) probabilities. This quantity is only inferred for the time range 128 - 117ka (see Materials and Methods). b-d. Local sea level model posteriors (shading showing central 68% and 95% probabilities, as in a.) for specific regions in the database. Note that data elevations have been corrected for longterm uplift and markers show the most likely posterior age.

Science Advances Manuscript Template Page 26 of 29

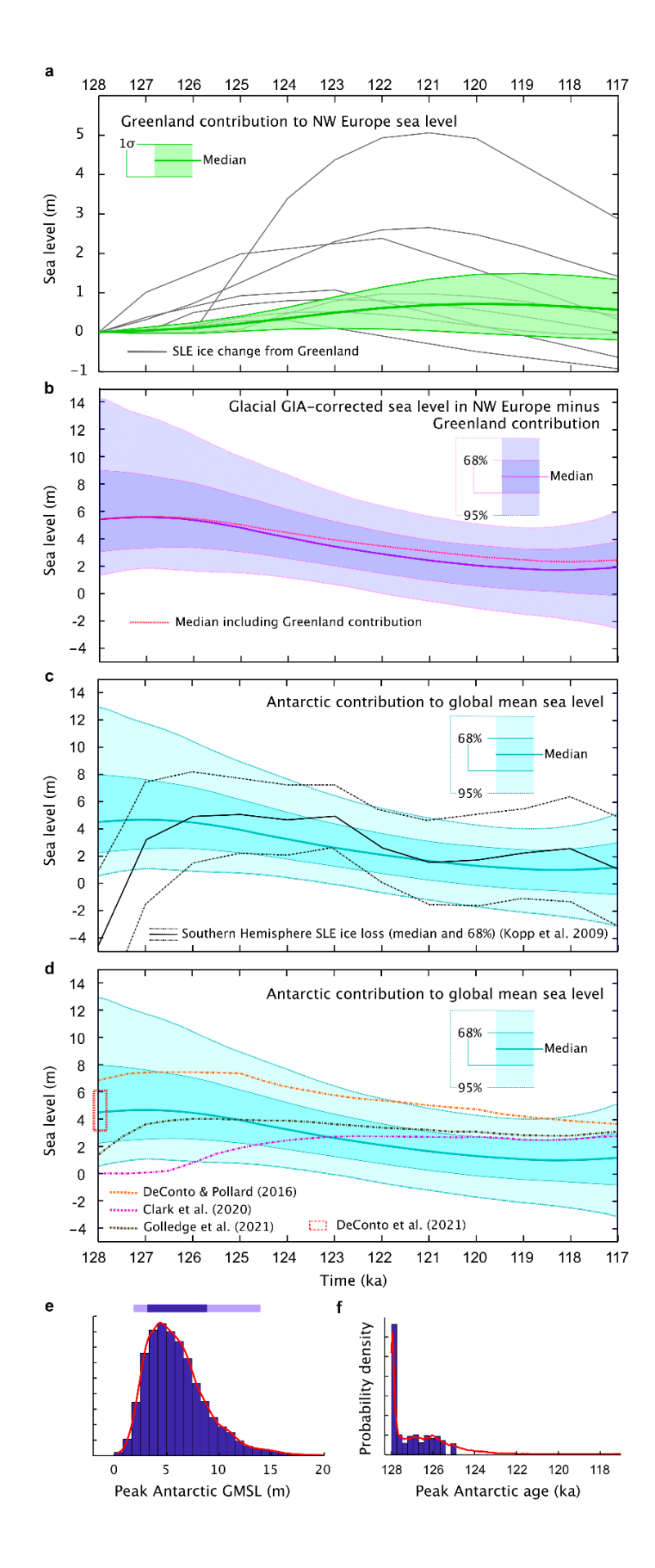


Fig. 3 | Greenland and Antarctic contributions to Last Interglacial sea level. a. Greenland Ice Sheet models (n=8; grey lines) showing global sea-level equivalent contributions from the ice sheet (grey), and the resulting mean $(\pm 1\sigma)$ time-varying sea-level rise in NW Europe (green line and shading). b. Glacial GIA-corrected LIG sea level in NW Europe with the Greenland component (a) removed. c. The Antarctic contribution to global LIG by removing contributions from glaciers and thermal expansion from b and accounting for the GIA signal of Antarctic mass loss. The global Antarctic contribution is compared against sea-level equivalent ice loss from the Southern Hemisphere (20) in c, and compared against sea-level equivalent mass loss from Antarctica after (19, 47, 48), and against the target range of LIG Antarctic sea-level equivalent mass loss used to parametrize projection models (6) in d. e-f. Probability density functions of the magnitude (e.) and timing (f.) of peak Antarctic contributions to global mean sea level during the LIG.

Table 1. Absolute-dated Last Interglacial relative sea-level data from NW Europe including regional weighted means (see also Supplementary Data)

| ID Location | | Feature | Age | *RWL (± IR/2) | *RSL | |
|-------------------|---|---|---------------------|-------------------|--------------------|--|
| | | | $(ka, \pm 1\sigma)$ | | $(m, \pm 1\sigma)$ | |
| DK1 | Jutland Shoreface- Glaciofluvial sands | | 106 ± 11 | 2.0 (T.limiting) | 16.0 (T.limiting) | |
| DK2 | Jutland | Beach deposits | 121 ± 13 | -0.1 ± 0.24 | 18.1 ± 0.47 | |
| FR1 | Normandy | Dune sands | 106 ± 10 | 6.4 (T.limiting) | -1.4 (T.limiting) | |
| FR3 | Normandy | Dune sands | 107 ± 10 | 10.5 (T.limiting) | -4.5 (T.limiting) | |
| | Normandy | MIS 5d weighted mean (limiting): | 107 ± 7 | | ≤ -3.0 | |
| FR5 | Normandy | Dune sands | 111 ± 8 | 5.9 (T.limiting) | 1.4 (T.limiting) | |
| FR7 | Normandy | Dune sands | 115 ± 12 | 5.9 (T.limiting) | 3.9 (T.limiting) | |
| | Normandy | MIS 5e weighted mean (limiting): | 112 ± 7 | | \leq 2.7 | |
| FR2 | Normandy | Beach deposits | 115 ± 11 | 1.4 ± 2.7 | 4.6 ± 2.7 | |
| FR4 | Normandy | Beach ridge | 118 ± 12 | 4.1 ± 1.8 | 3.6 ± 1.9 | |
| FR6 | Normandy | Beach ridge | 121 ± 13 | 4.1 ± 1.8 | 5.7 ± 1.9 | |
| | Normandy N | MIS 5e weighted mean: | 118 ± 7 | | 4.6 ± 1.2 | |
| FR8 | Normandy | Marine sands | 126 ± 11 | -0.1 ± 2.1 | 0.4 ± 2.1 | |
| UK1 | Yorkshire | Dune sands | 121 ± 12 | 11.8 (T.limiting) | -7.8 (T.limiting) | |
| UK2 | Sussex Marine sediments | | 121 ± 12 | 0.0 ± 1.7 | 5.0 ± 1.7 | |
| UK3 | Sussex Marine sediments | | 124 ± 10 | 0.0 ± 1.6 | 5.0 ± 1.7 | |
| UK4 | Sussex Beach ridge | | 133 ± 13 | 4.9 ± 2.7 | 2.1 ± 2.7 | |
| UK5 | I. of Wight | Estuarine sediments | 115 ± 10 | 0.0 ± 1.3 | 6.0 ± 1.3 | |
| UK6 | Wales | Vales Beach ridge 122 ± 9 7.6 ± 3 . | | 7.6 ± 3.7 | 5.4 ± 3.7 | |
| UK7 | Wales Beach ridge | | 117 ± 23 | 7.6 ± 3.7 | 4.8 ± 3.7 | |
| | Wales I | MIS 5e weighted mean: | 121 ± 8 | | 5.1 ± 2.6 | |
| UK8 | Jersey | Beach deposits | 121 ± 14 | 1.3 ± 2.9 | 6.7 ± 2.9 | |
| UK9 | Devon | Marine sediments | 116 ± 9 | -0.1 ± 1.5 | 5.8 ± 1.5 | |
| UK10 [†] | Cornwall | Beach deposits | 120 ± 7 | 0.3 ± 2.6 | 4.8 ± 2.7 | |

Science Advances Manuscript Template Page 28 of 29

| UK11 [†] | Cornwall | Beach deposits (notch) | 119 ± 7 | -0.1 ± 2.0 | 4.8 ± 2.0 |
|-------------------|------------|------------------------|-------------|-------------------|-------------------|
| UK12 [†] | Cornwall | Beach deposits | 115 ± 6 | 0.4 ± 2.6 | 4.6 ± 2.6 |
| UK13 [†] | Cornwall | Beach deposits (notch) | 115 ± 6 | -0.1 ± 2.1 | 4.5 ± 2.1 |
| $UK14^{\dagger}$ | Cornwall | Beach deposits | 141 ± 12 | 0.3 ± 2.9 | 6.1 ± 2.9 |
| UK15 [†] | Cornwall | Beach deposits | 131 ± 14 | 0.3 ± 2.9 | 5.6 ± 2.9 |
| $UK16^{\dagger}$ | Cornwall | Beach deposits | 123 ± 12 | 0.3 ± 2.9 | 4.5 ± 2.9 |
| | Cornwall 1 | MIS 5e weighted mean: | 119 ± 3 | | 4.9 ± 1.0 |
| UK17 | Cornwall | Dune sands | 116 ± 9 | 11.3 (T.limiting) | -3.3 (T.limiting) |

Page 29 of 29 Science Advances Manuscript Template

^{*} RWL – reference water level; IR – indicative range; RSL – relative sea level

† New age constraints developed in this study
T.limiting = terrestrial limiting data point (i.e. sea level was lower than this elevation)



Supplementary Materials for

Constraining the contribution of the Antarctic Ice Sheet to Last Interglacial sea-level

Robert Barnett, Jacqueline Austermann, et al.

*Corresponding author. Email: jackya@ldeo.columbia.edu

This PDF file includes:

Figs. S1 to S9 Tables S1 to S2

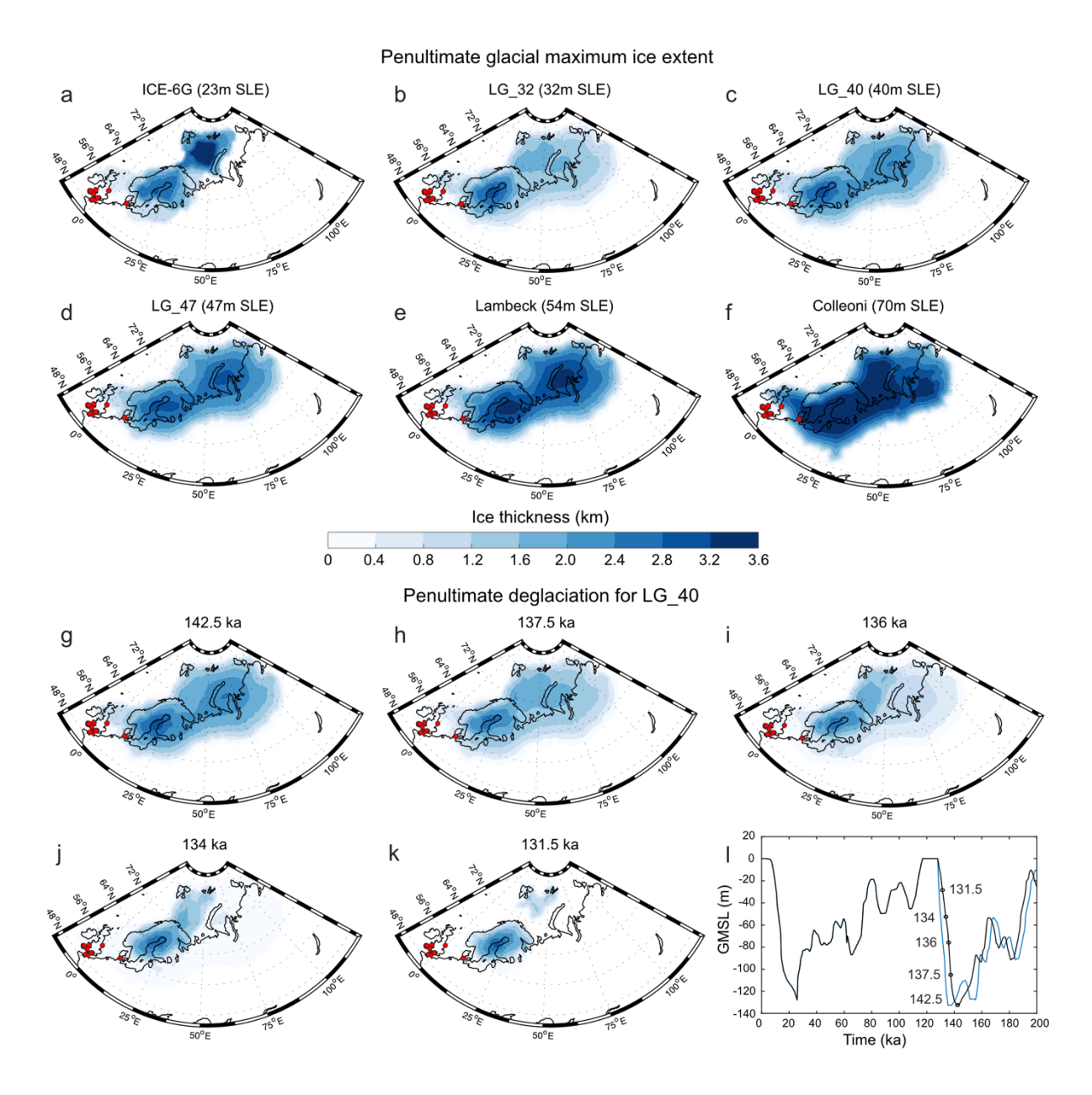


Fig. S1. Suite of Eurasian ice sheet configurations used in the glacial GIA model. a.-f. Eurasian ice sheet at the penultimate glacial maximum for a series of reconstructions with varying ice sheet size (see Methods for details). The sea level equivalent (SLE) of each ice sheet that is indicative of the ice volume is shown on the figure. Data locations are shown by red markers. g.-k. Eurasian ice sheet collapse over the penultimate deglaciation for one ice scenario (LG_40). The resulting GIA response during the LIG is shown in Fig. 1c, d. l. Global mean sea level change over the past 200 ka assuming a faster (blue) or slower (black) deglaciation. Highlighted ages correspond to ice configurations shown in panels g-k.

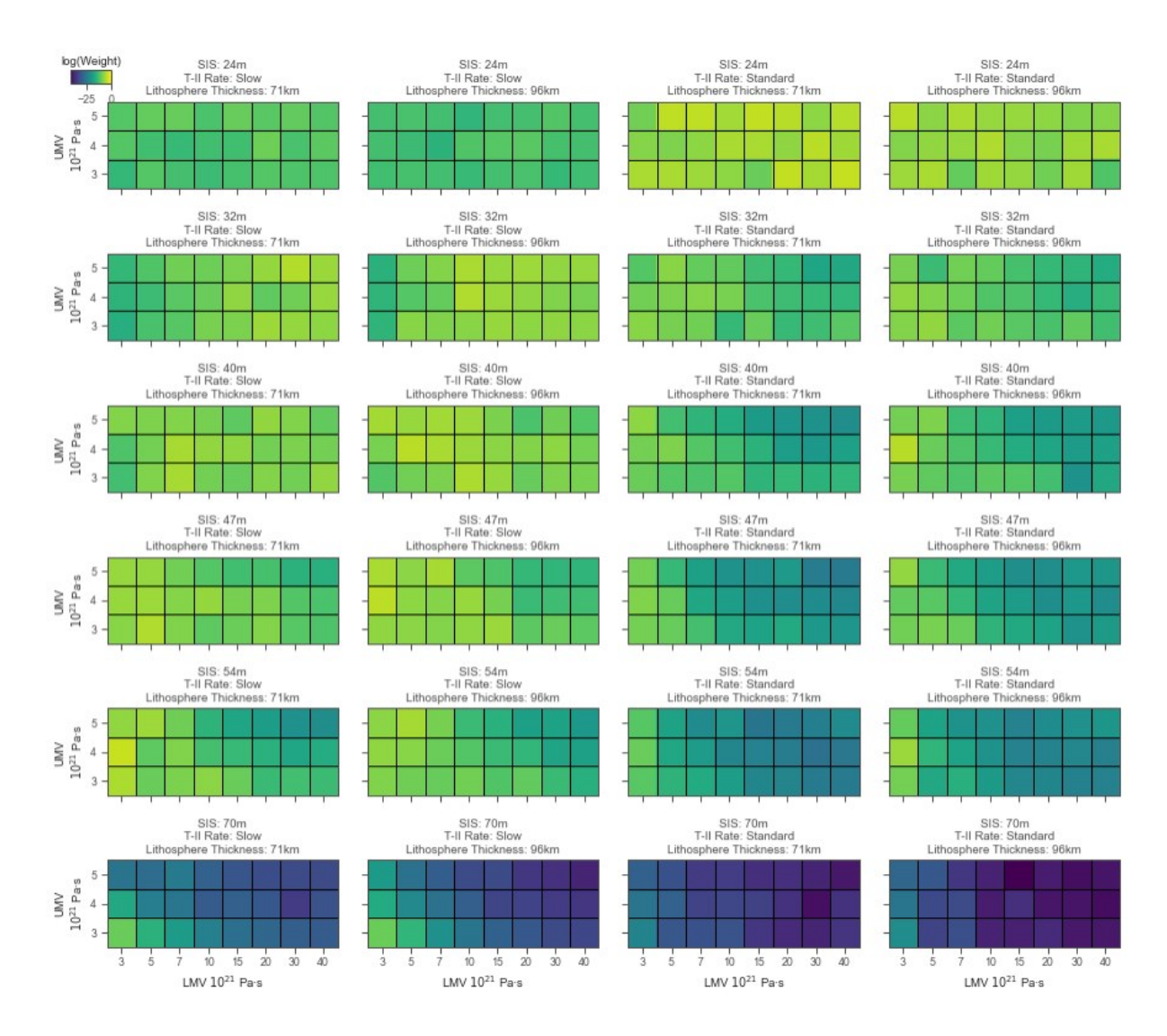


Fig. S2. Performance of glacial GIA model suite. Model weights for the 576 different glacial GIA models based on model fit to RSL data.

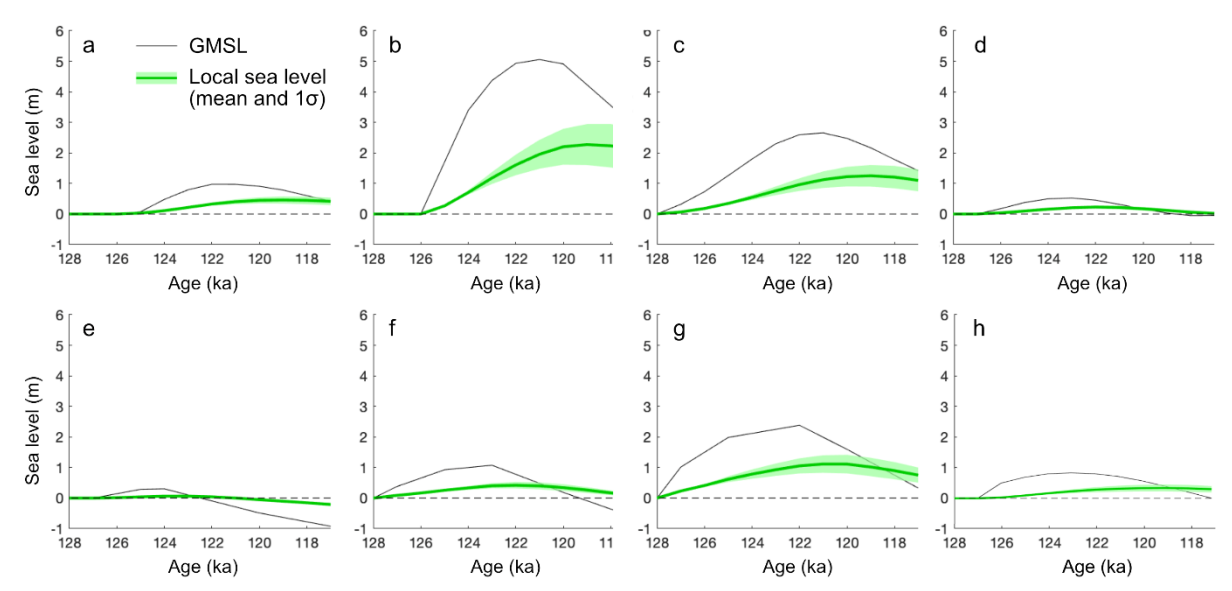


Fig. S3. Local sea level in northwest Europe in response to Greenland mass loss. a. Greenland contribution to GMSL change over the LIG (black) from Quiquet et al. (2013). Note that we only start adopting the model once it reaches an ice volume below present values. Local sea level in northwest Europe as a result of this ice model is shown in green for varying viscosity models (mean and 1σ). b. Same as a but for the ice history by Yau et al. (2016). c, d. Same as a but for the two ice scenarios by Calov et al. (2015). e-g. Same as a but for the ice histories by Goelzer et al. (2016). h. Same as a but for the ice history by Bradley et al. (2018).

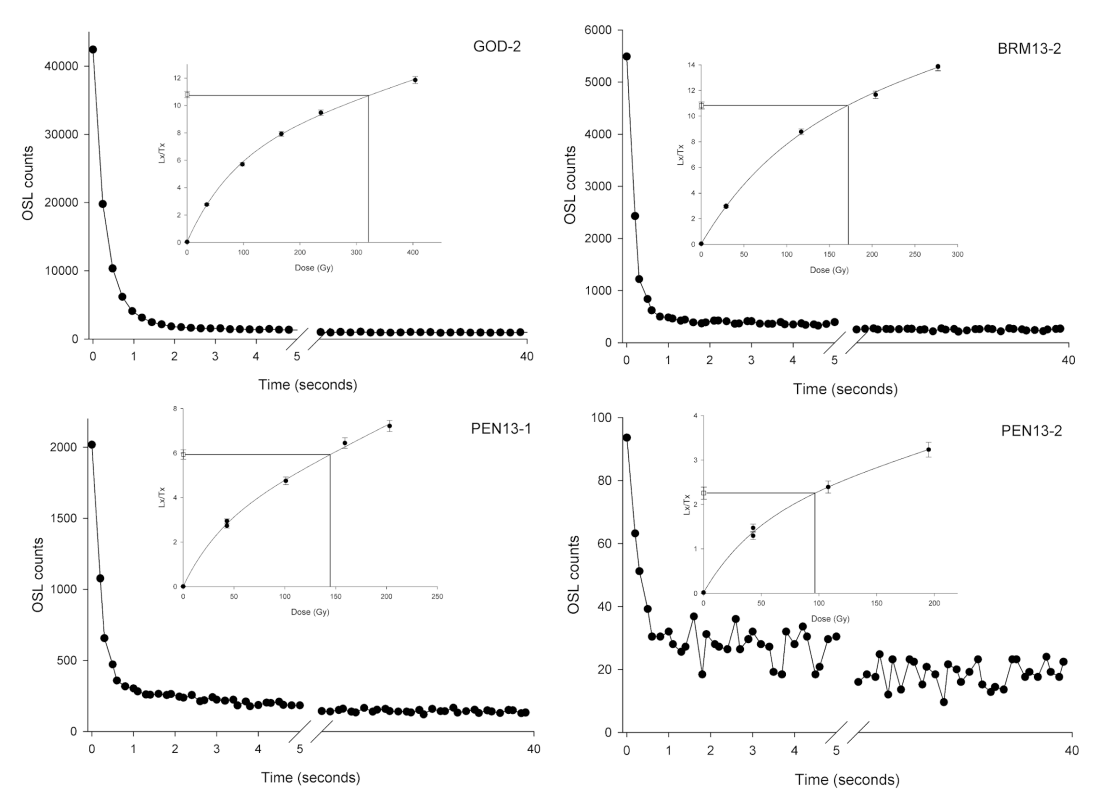


Fig. S4. Examples of quartz OSL shine down curves and dose-response curves. All measurements are on 2 mm diameter aliquots of $180\text{-}212~\mu m$ grains, and are in response to an 11 Gy test dose. Accompanying dose-response curves are fitted with a saturating exponential plus linear equation (I=I0(1-exp[-D/D0])+kD where I = luminescence intensity, I0 = Maximum luminescence intensity, D = Dose (Gy), D0 = characteristic dose (Gy) and k is the constant for the linear term). In the case of PEN13-2 a different (more sensitive) aliquot was used to generate the dose-response curve shown in the inset figure.

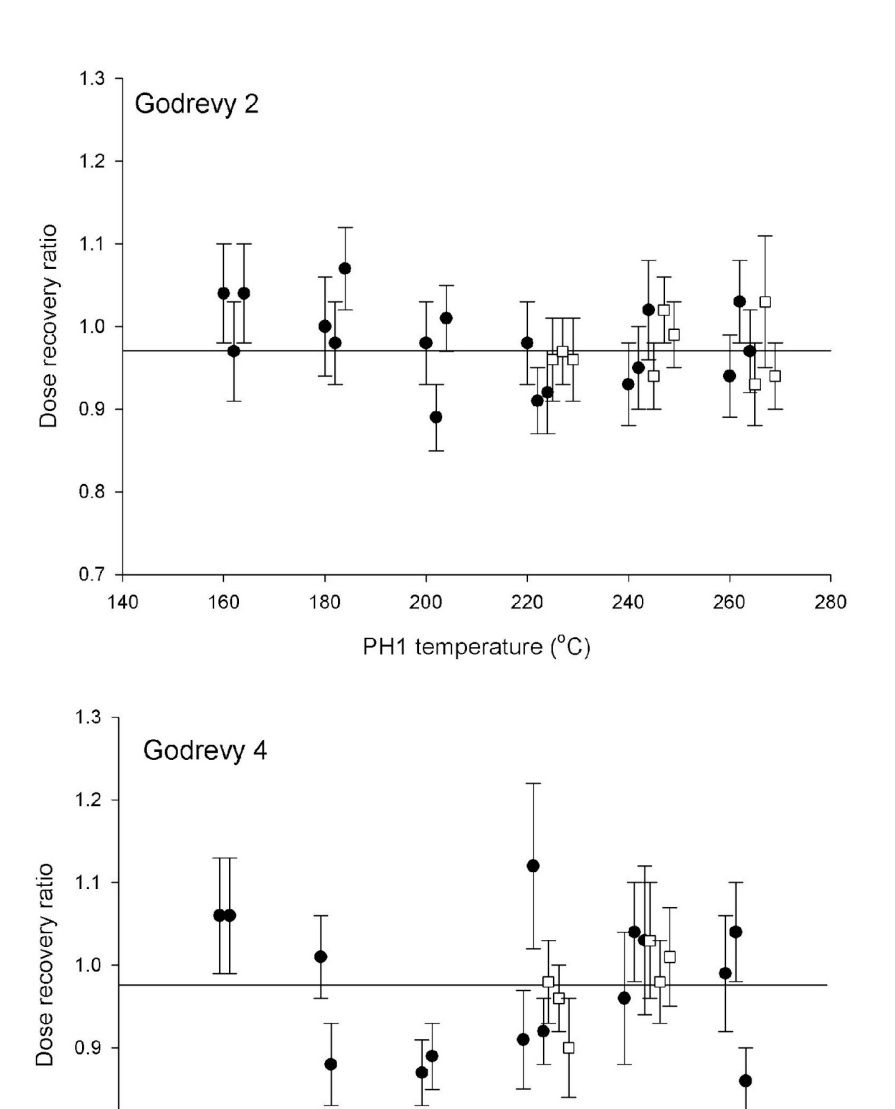
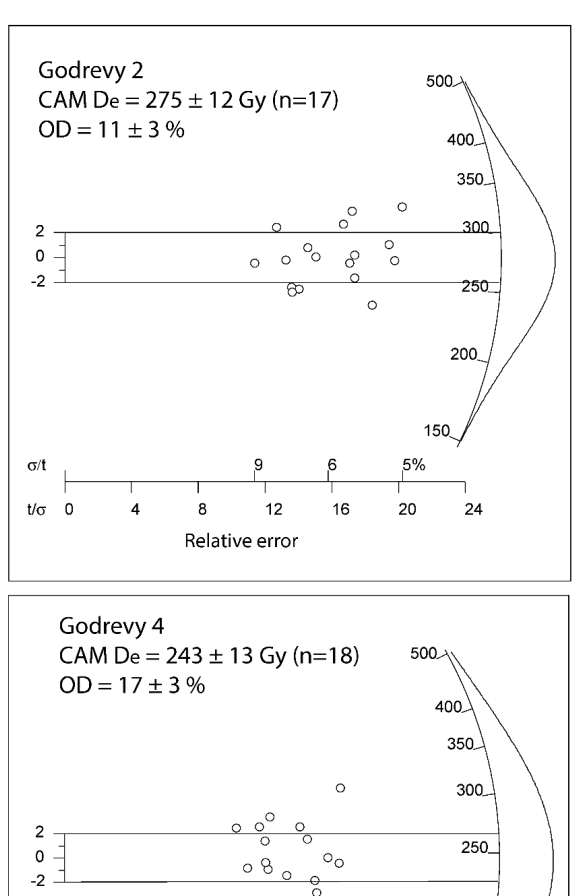


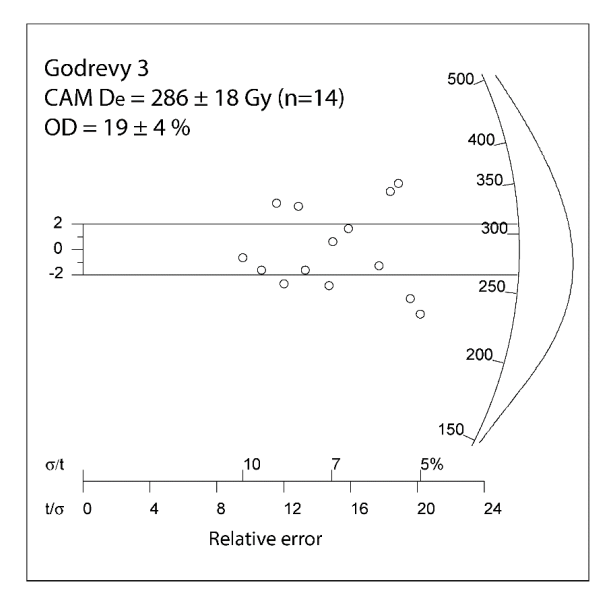
Fig. S5. Dose recovery preheat experiments results for Godrevy 2 and 4. The black data points utilised a 160°C cut heat test dose preheat, while the open data points utilized a 220°C cut heat test dose preheat. The horizontal line shows the mean dose recovery ratio for all aliquots. The administered dose was 98 Gy in both cases.

PH1 temperature (°C)

0.8

0.7





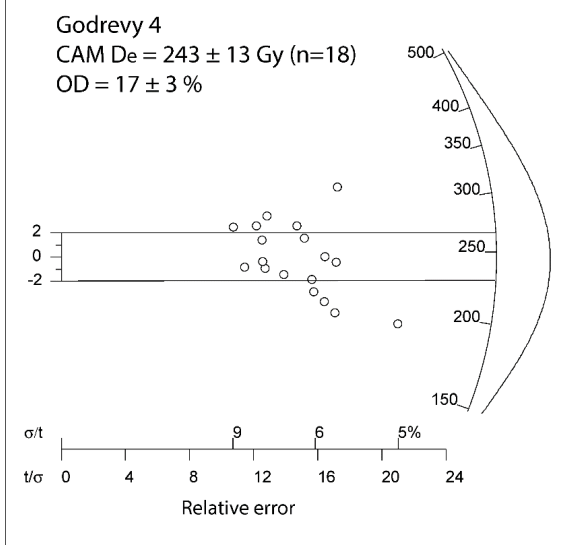


Fig. S6. Radial plots (with accompanying Abanico plot) showing the equivalent dose distributions for the quartz SAR analyses of the Godrevy samples.

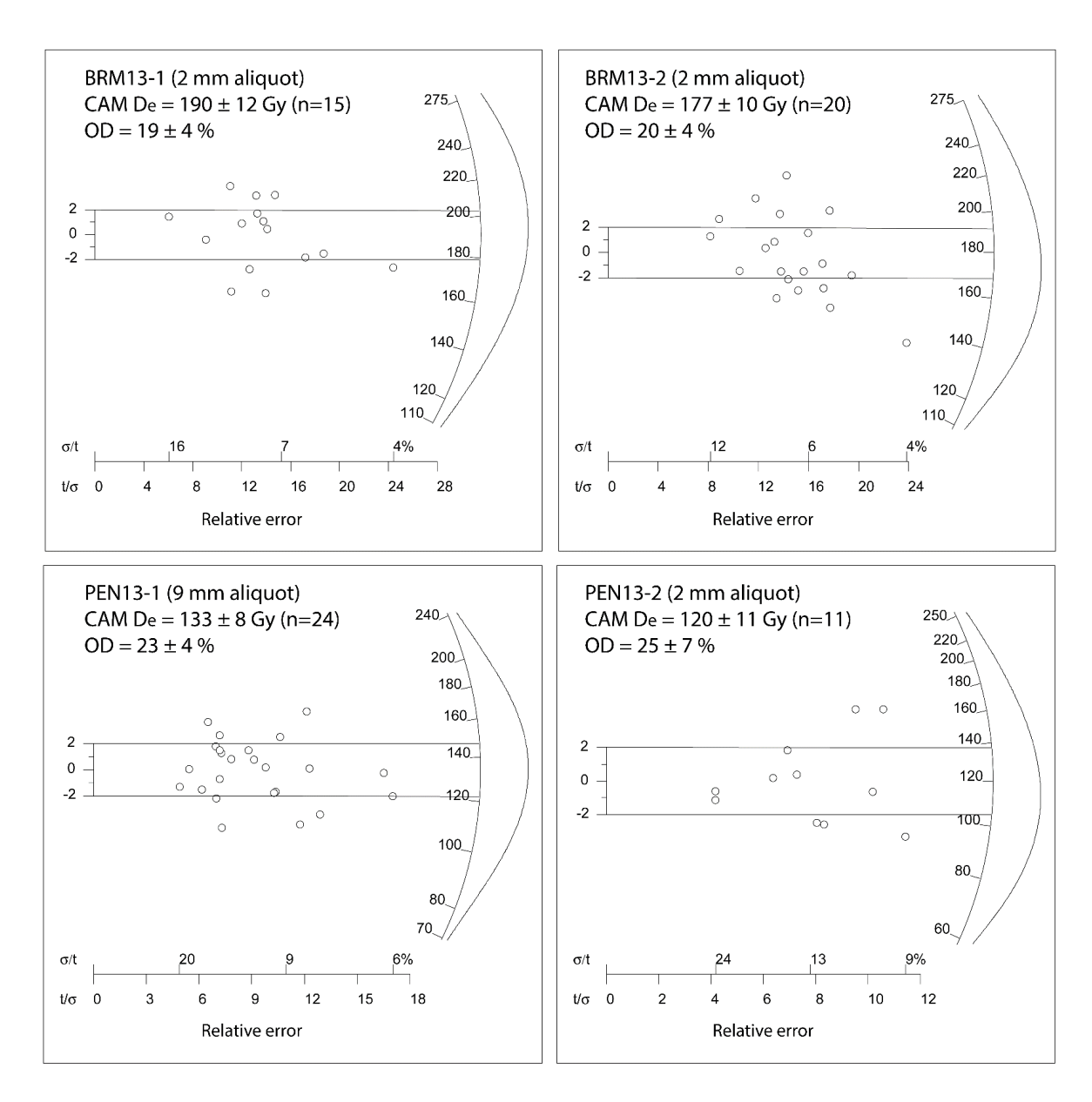


Fig. S7. Radial plots (with accompanying Abanico plot) showing the equivalent dose distributions for the quartz SAR analyses of the Pedower and Bream Cove.

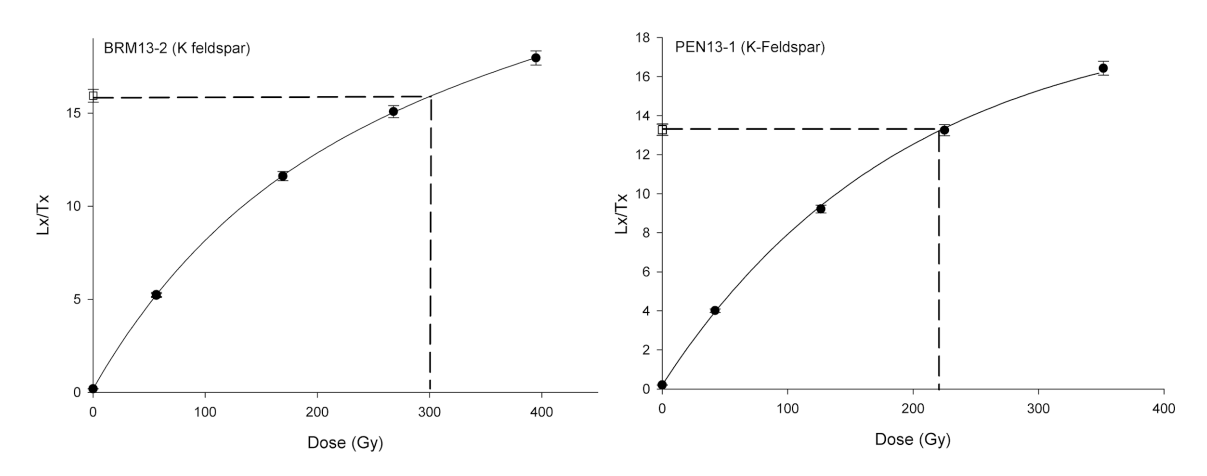


Fig. S8. Exemplar K-feldspar dose-response curves for the pIRIR₁₇₀ measurements conducted on the Bream Cover and Pendower samples. The data are fitted with saturating exponential fits.

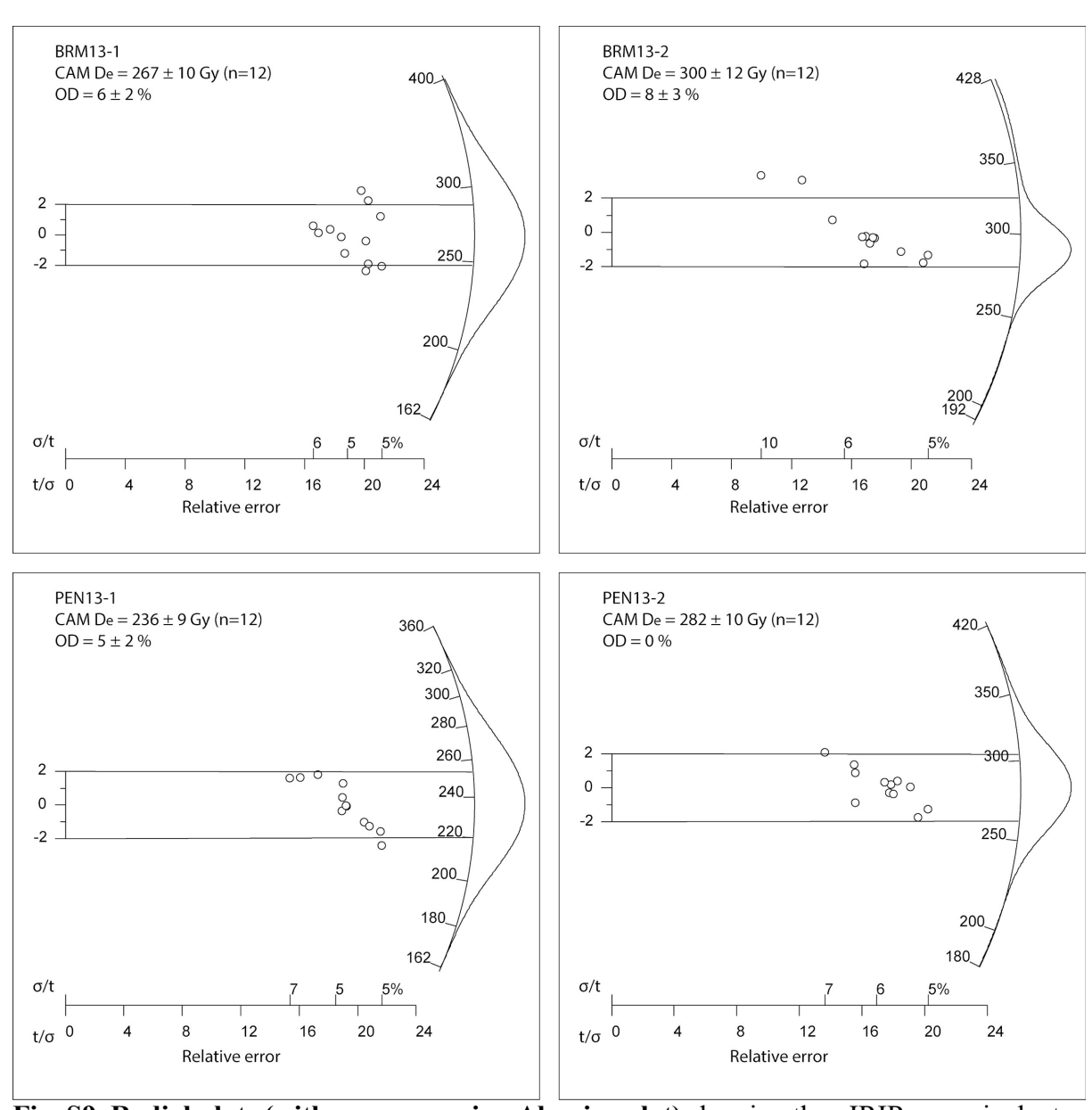


Fig. S9. Radial plots (with accompanying Abanico plot) showing the pIRIR₁₇₀ equivalent dose distributions for the Pedower and Bream Cove samples

Table S1. Details of the quality control checks on the luminescence dating analyses. For quartz these include details of the dose recovery experiments with varying preheating conditions. For K-feldspar these include dose recovery ratios, and measured residuals following daylight exposure (c. 48 hours), as well as the results of anomalous fading rate analyses.

| Sample | Field ID | Method | Dose recovery ratio (n) | Mean Recycling ratio | Mean Recuperatio n (%) | Chosen preheat temperatur e (°C) | DR ratio for selected preheat combination (n) | | | |
|--------|----------|-------------------|-------------------------------|----------------------------|------------------------------|---|---|---------------------------------------|---------------------------------------|---|
| | | | | | | | | | | |
| UK14 | GOD12-2 | Quartz OSL | 0.98 ± 0.04 (27) | 1.00 ± 0.03 | 0.5 ± 0.3 | 240/220 | 0.99 ± 0.04 (3) | | | |
| UK15 | GOD12-3 | Quartz OSL | 1.04 ± 0.05 (6) | 1.00 ± 0.01 | 0.8 ± 0.3 | 240/220 | 1.01 ± 0.03 (3) | | | |
| UK16 | GOD12-4 | Quartz OSL | 0.98 ± 0.09 (21) | 1.00 ± 0.04 | 0.4 ± 0.2 | 240/220 | 0.99 ± 0.01 (3) | | | |
| UK10 | BRM13-1 | Quartz OSL | 1.02 ± 0.07 (17) | 1.00 ± 0.03 | 0.3 ± 0.2 | 220/160 | 1.00 ± 0.01 (3) | | | |
| UK11 | BRM13-2 | Quartz OSL | 1.02 ± 0.05 (17) | 1.00 ± 0.03 | 0.4 ± 0.3 | 240/160 | 1.04 ± 0.03 (3) | | | |
| | | | | | | | | | | |
| | | | De IR50 (Gy) | De pIRIR170 (Gy) | De pIRIR225 (Gy) | Residual pIRIR ₁₇₀ (Gy) | Residual pIRIR225 (Gy) | Dose recovery ratio pIRIR170 | Dose recovery ratio pIRIR225 | g-value2days pIRIR170 (% per decade) |
| UK10 | BRM13-1 | Feldspar pIRIR | 171 ± 6 | 267 ± 10 | 258 ± 9 | 17 | 22 | 1.05 ± 0.01 | 0.93 ± 0.02 | 1.25 ± 0.41 |
| UK11 | BRM13-2 | Feldspar pIRIR | 176 ± 6 | 300 ± 12 | 272 ± 9 | 12 | 21 | 0.96 ± 0.01 | 0.90 ± 0.01 | 0.99 ± 0.61 |
| UK13 | PEN13-1 | Feldspar pIRIR | 148 ± 5 | 236 ± 9 | nd* | nd* | nd* | 1.04 ± 0.01 | nd* | 1.14 ± 0.63 |
| UK12 | PEN13-2 | Feldspar pIRIR | 178 ± 6 | 282 ± 10 | nd* | 16 | 23 | 1.03 ± 0.01 | 0.87 ± 0.05 | 1.29 ± 0.42 |

Table S2. Details of the dose rate determinations as obtained using in-situ gamma spectrometry. The total dose rate for the K-feldspar (un-etched samples) analyses also includes an external alpha dose rate contribution. The internal beta dose to K-feldspar assumes a K content of 12.5 ± 0.5 % and an Rb content of 400 ± 100 ppm (see Materials and Methods).

| | | Dosimetr | y | | | Equivalent dose determination | | | | | |
|---------------------------------|----------|-------------|-----------------|----------------|--|--|--|-----------------------------------|---------------------|--------------|--------------|
| Sample code | Field ID | K (%) | U (ppm) | Th (ppm) | Cosmic dose (Gy ka ⁻¹) | Internal dose (Gy ka ⁻¹) | Total dose rate (Gy ka ⁻¹) | Aliquots accepted/ analyzed | Overdis persion (%) | De (Gy) | Age (ka) |
| | Quartz | | | | | | | | | | |
| UK14 | GOD12-2 | 1.51 ± 0.08 | 1.49 ± 0.15 | 5.92 ± 0.59 | 0.08 ±0.01 | n/a | 1.94 ± 0.15 | 17/17 | 11.1 | 275 ± 12 | 141 ± 12 |
| UK15 | GOD12-3 | 1.82 ± 0.09 | 1.3 ± 0.13 | 6.5 ± 0.65 | 0.08 ±0.01 | n/a | 2.19 ± 0.17 | 14/18 | 18.9 | 295 ± 21 | 135 ± 14 |
| UK16 | GOD12-4 | 1.71 ± 0.09 | 1.23 ± 0.12 | 4.61 ± 0.46 | 0.08 ±0.01 | n/a | 1.97 ± 0.16 | 18/18 | 16.8 | 244 ± 13 | 123 ± 12 |
| UK10 | BRM13-1 | 0.95 ± 0.05 | 1.13 ± 0.06 | 4.55 ± 0.23 | 0.12 ±0.01 | n/a | 1.38 ± 0.12 | 15/15 | 19.2 | 190 ± 12 | 138 ± 13 |
| UK11 | BRM13-2 | 1.05 ± 0.05 | 2.21 ± 0.11 | 4.62 ± 0.23 | 0.12 ±0.03 | n/a | 1.67 ± 0.12 | 20/20 | 20.4 | 178 ± 10 | 107 ± 8 |
| UK13 | PEN13-1 | 0.75 ± 0.04 | 1.17 ± 0.12 | 2.82 ± 0.28 | 0.18 ±0.02 | n/a | 1.18 ± 0.08 | 24/35 | 25.2 | 133 ± 8 | 113 ± 10 |
| UK12 | PEN13-2 | 0.81 ± 0.04 | 2.37 ± 0.12 | 5.22 ± 0.26 | 0.18 ±0.02 | n/a | 1.61 ± 0.11 | 11/30 | 23.3 | 120 ± 11 | 75 ± 9 |
| | | | | | | | | | | | |
| K-feldspar pIRIR ₁₇₀ | | | | | | | | | | | |
| UK10 | BRM13-1 | 0.95 ± 0.05 | 1.13 ± 0.06 | 4.55 ± 0.23 | 0.12 ±0.01 | 0.85 | 2.23 ± 0.11 | 12/12 | 6.4 | 267 ± 10 | 120 ± 7 |
| UK11 | BRM13-2 | 1.05 ± 0.05 | 2.21 ± 0.11 | 4.62 ± 0.23 | 0.12 ±0.03 | 0.85 | 2.52 ± 0.11 | 12/12 | 7.6 | 300 ± 12 | 119 ± 7 |
| UK13 | PEN13-1 | 0.75 ± 0.04 | 1.17 ± 0.12 | 2.82 ± 0.28 | 0.18 ±0.02 | 0.85 | 2.05 ± 0.08 | 12/12 | 4.6 | 236 ± 9 | 115 ± 6 |
| UK12 | PEN13-2 | 0.81 ± 0.04 | 2.37 ± 0.12 | 5.22 ± 0.26 | 0.18 ±0.02 | 0.85 | 2.46 ± 0.11 | 12/12 | 0 | 282 ± 10 | 115 ± 6 |